Traveling waves and defects in the complex Swift-Hohenberg equation

Lendert Gelens[1,*] and Edgar Knobloch[2,†]
[1]*Applied Physics Research Group (APHY), Vrije Universiteit Brussel, Pleinlaan 2, B-1050 Brussel, Belgium*
[2]*Department of Physics, University of California, Berkeley, California 94720, USA*
(Received 21 June 2011; revised manuscript received 29 August 2011; published 7 November 2011)

The complex Swift-Hohenberg equation models pattern formation arising from an oscillatory instability with a finite wave number at onset and, as such, admits solutions in the form of traveling waves. The properties of these waves are systematically analyzed and the dynamics associated with sources and sinks of such waves investigated numerically. A number of distinct dynamical regimes is identified and analyzed using appropriate phase equations describing the evolution of long-wavelength instabilities of both the homogeneous oscillating state and constant amplitude traveling waves.

DOI: 10.1103/PhysRevE.84.056203 PACS number(s): 05.45.−a, 42.65.Sf

I. INTRODUCTION

Spatially extended systems in many areas of physics exhibit spontaneous pattern formation when driven away from equilibrium [1–3]. The patterns that result can be classified according to the linear instability of the spatially uniform system that creates them. By increasing a control parameter beyond a critical value this homogeneous equilibrium state may lose stability with respect to perturbations with a characteristic wave vector $\mathbf{k}_0$ and/or with a characteristic frequency ω_0 at the instability threshold. Near this threshold the system can often be described by simpler, generic equations [3–5].

The complex Swift-Hohenberg equation (CSHE) is one such universal equation that models pattern formation arising from an oscillatory instability ($\omega_0 \neq 0$) with a finite wave number ($k_0 \neq 0$) at onset [6,7]. The Swift-Hohenberg equation was originally obtained in the context of thermal convection problems [8], but also finds applications in Couette flow [9], magnetoconvection [10], liquid crystals [11], flame dynamics [12], and nonlinear optics [13–20].

In this work, we focus on the application of the CSHE in the field of nonlinear optics. The derivation of the CSHE model has been discussed in the context of optical parametric oscillators (OPOs) [13–15,21,22], photorefractive oscillators [16], and lasers [17–20]. When studying transverse dynamics in large-aspect-ratio laser systems, the Maxwell-Bloch equations provide a good description of pattern formation in single longitudinal mode, two-level lasers. The behavior of the laser system is then largely determined by the cavity detuning ν, which is directly related to the difference between the atomic frequency and the closest cavity resonance frequency. In the case of negative detuning ($\nu < 0$), Coullet *et al.* [23] showed that the laser dynamics close to threshold could be described by a complex Ginzburg-Landau equation (CGLE). In the case of positive detuning ($\nu > 0$), Newell and Moloney [24] derived coupled Newell-Whitehead-Segel–like equations to describe two-dimensional dynamics close to threshold. In one dimension the latter equations reduce to two coupled complex Ginzburg-Landau equations (CCGLEs) describing the interaction between two counterpropagating traveling waves [25]. For a detailed study of the CCGLEs we refer to Ref. [26]. A more general description of class A and C lasers for both signs of the detuning ν is given by the CSHE as shown by Lega *et al.* [17,18]. The validity of the CSHE as an approximation to the general Maxwell-Bloch equations is evaluated in Ref. [27]. The CSHE description of two-level lasers has been generalized to model semiconductor lasers [19] and its validity in this context has also been investigated [28,29].

In this paper we study the properties of the supercritical CSHE in one spatial dimension, viz.,

$$u_t = ru + i\zeta u_{xx} - (1+i\beta)\left(\partial_x^2 + k_0^2\right)^2 u - (1+ib)|u|^2 u, \tag{1}$$

where u is a complex field representing the amplitude of a traveling wave in a frame moving with the group velocity. In optics applications u typically represents the complex amplitude of a transverse electric field, for example, inside a laser cavity.

The equation is fully parametrized by four real parameters r, ζ, β, and b [6,7,17,18]. We treat the parameter r as a bifurcation parameter, focusing on the behavior of the solutions as a function of the parameter β, for fixed values of the parameters b and ζ. We remark that in many applications (e.g., Refs. [13–20]) the parameter β vanishes, although in others (e.g., Ref. [29]) β may differ from zero. On the real line the remaining parameter, the wave number k_0, can be scaled out of the problem, but we prefer to retain it in the formulation in order to emphasize the role played by the intrinsic length scale in the problem. The traveling wave solutions of Eq. (1) can be thought of as generalizations of the time-independent phase-winding states studied in previous work on the CSHE with real coefficients [30]; when $\zeta = \beta = b = 0$ such states cannot travel because the equation has variational structure.

Our goal in this work is to provide a systematic study of the generic CSHE, focusing on defects associated with the presence of traveling waves, that is, sources and sinks of traveling waves, and on their stability properties. The work can be thought of as an extension of related studies of the CGLE [1,5,31–33] in which the intrinsic length scale $2\pi/k_0$ is infinite. The formation of defects is an inevitable consequence of random initial conditions that are commonly used in simulations of both CSHE and CGLE. A typical

*lendert.gelens@vub.ac.be
†knobloch@berkeley.edu

solution consists of domains in which the waves propagate in one or other direction. These domains are separated by (typically moving) defects: sources that send out TW and sinks that absorb them [34–37]. Over time the defects can annihilate or new defects can be created. In addition, defects can undergo a variety of instabilities leading, for example, to breathing or chaotic motion, or they may form bound states that propagate through the system with a common speed. Sinks and sources differ in general in their properties, with sinks often stable and sources prone to instabilities [26,34,36]. In the field of nonlinear optics, for example, in laser systems, sources, and sinks have been studied in Refs. [38–40].

Our analysis of traveling waves and defects between these waves provides a comparison with other much used universal equations, such as the CGLE and the CCGLEs. We also show that there exists an intimate connection between the CSHE and the Cahn-Hilliard and Korteweg-de Vries equations. The Cahn-Hilliard equation was originally derived to describe the dynamics of phase separation in systems with a conserved quantity in the context of binary alloys [41], but it also describes coarsening dynamics observed in many other areas of physics. The Korteweg-de Vries equation was derived to model shallow-water waves and is one of the prototypical soliton-bearing equations [42]. We show that both equations arise naturally as evolution equations for wave number perturbations of solutions of Eq. (1) in the form of nonlinear wave trains and relate their solutions to direct numerical simulations of perturbed wave trains.

The paper is organized as follows. In Sec. II we describe the properties of simple traveling wave (TW) solutions of the CSHE and show that such waves are subject to long-wavelength instabilities. In Sec. III we study the properties of defects between such waves and describe the similarities and differences between the behavior of the CSHE and a pair of CCGLEs describing the dynamics near onset. In Sec. IV we present the results of numerical simulations of the CSHE in a variety of different parameter regimes. In Sec. V we derive phase equations describing the evolution of long-wavelength instabilities of both the homogeneous oscillating state and the TW states identified in Sec. II. For the former the phase equation takes the form of a generalized convective Cahn-Hilliard equation that describes both coarsening behavior and spatiotemporal chaos. For the latter the phase equation takes the form, in appropriate regimes, of a perturbed Korteweg-de Vries equation describing localized compression or dilation of the TW. The paper concludes with a brief conclusion in Sec. VII.

II. TRAVELING WAVE SOLUTIONS

Equation (1) has a nonzero homogeneous solution of the form

$$u(x,t) = u_0 \exp i\Omega t, \tag{2}$$

where

$$|u_0|^2 = r - k_0^4, \quad \Omega = -br + (b-\beta)k_0^4. \tag{3}$$

The stability of this solution is determined by writing $u(x,t) = u_0[1+\delta(x,t)]\exp i\Omega t$ and linearizing in the small perturbation $\delta(x,t)$. The perturbation then evolves according to the equation

$$\begin{aligned}\delta_t = {} & \left[i\zeta - 2k_0^2(1+i\beta)\right]\delta_{xx} - (1+i\beta)\delta_{xxxx} \\ & - (1+ib)|u_0|^2(\delta+\bar{\delta}).\end{aligned} \tag{4}$$

This equation is solved using the ansatz $\delta(x,t) = \delta_+ \exp(\sigma t + ikx) + \bar{\delta}_- \exp(\sigma t - ikx)$ leading to the dispersion relation

$$\begin{aligned}&\left(\sigma - 2k_0^2k^2 + k^4 + |u_0|^2\right)^2 + \left[k^2\left(\zeta - 2k_0^2\beta\right) + \beta k^4 + b|u_0|^2\right]^2 \\ &- (1+b^2)|u_0|^4 = 0.\end{aligned} \tag{5}$$

The two roots $\sigma_\pm$ of this equation are shown in Fig. 1 as a function of the perturbation wave number k. One of the roots, σ_-, is always negative (stable) while the other, σ_+, may be positive for small k (long-wavelength instability). This root is given explicitly by

$$\begin{aligned}\sigma_+ = {} & \left(2k_0^2 - b\zeta + 2b\beta k_0^2\right)k^2 \\ & - \left[1 + b\beta + \frac{1+b^2}{2|u_0|^2}\left(\zeta - 2k_0^2\beta\right)^2\right]k^4 + \cdots,\end{aligned} \tag{6}$$

implying that the homogeneous oscillation $u_0 \exp i\Omega t$ is unstable with respect to long-wavelength perturbations when

$$1 + b\beta > b\zeta/2k_0^2. \tag{7}$$

This condition is similar to the condition for the presence of the Benjamin-Feir instability of the Stokes solution of the CGLE, except that here the instability is suppressed ($b\zeta > 0$) or enhanced ($b\zeta < 0$) depending on the sign of the product $b\zeta$. In particular, in the former case instability may be absent for small k_0 but present for larger k_0, indicating that the intrinsic scale of the problem has important consequences already for the simplest solution of the CSHE.

In addition to homogeneous oscillations the CSHE also admits solutions in the form of TWs. These take the form

$$u(x,t) = u_0 \exp(i\Omega t - iKx), \tag{8}$$

where

$$\begin{aligned}|u_0|^2 &= r - \left(k_0^2 - K^2\right)^2, \\ \Omega &= -br + (b-\beta)\left(k_0^2 - K^2\right)^2 - \zeta K^2.\end{aligned} \tag{9}$$

The stability of the TW solution is determined by writing $u(x,t) = u_0 \exp(i\Omega t - iKx)[1+\delta(x,t)]$, and linearizing in the small perturbation $\delta(x,t)$. The perturbation then evolves according to the equation

$$\begin{aligned}\delta_t = {} & \left[i\zeta - 2k_0^2(1+i\beta)\right](-2iK\delta_x + \delta_{xx}) - (1+i\beta)\left(4iK^3\delta_x\right. \\ & \left. - 6K^2\delta_{xx} - 4iK\delta_{xxx} + \delta_{xxxx}\right) - (1+ib)|u_0|^2(\delta+\bar{\delta}).\end{aligned} \tag{10}$$

This equation is solved using the ansatz $\delta(x,t) = \delta_+ \exp(\sigma t + ikx) + \bar{\delta}_- \exp(\bar{\sigma} t - ikx)$, where σ is now

complex. Although an exact expression for the real and imaginary parts of σ is readily obtained (see Fig. 2) we content ourselves with expressions for the (potentially) unstable eigenvalue σ_+ in the long-wavelength limit $k \ll 1$:

$$\mathrm{Re}\sigma_+ = \left[-b\zeta + 2(1+b\beta)\left(k_0^2 - 3K^2\right)\right]k^2 + \frac{8K^2k^2}{|u_0|^2}(1+b^2)\left(k_0^2 - K^2\right)^2 + O(k^4), \quad (11)$$

$$\mathrm{Im}\sigma_+ = 2Kk\left[\zeta + 2(b-\beta)\left(k_0^2 - K^2\right)\right] + O(k^3). \quad (12)$$

These expressions reduce to earlier expressions in the case $K = 0$. In contrast, when $K = k_0$ we obtain

$$\mathrm{Re}\sigma_+ = \left[-b\zeta - 4(1+b\beta)k_0^2\right]k^2 + O(k^4), \quad (13)$$

indicating that the TW and the homogeneous oscillations have, in general, different stability properties. In particular, it is possible for the TW with $K = k_0$ to be unstable while the homogeneous oscillations with $K = 0$ are stable, and vice versa. Moreover, when $K(k_0 - K) \neq 0$ the instability is enhanced by the second term in Eq. (11) and this term always dominates close to onset ($|u_0| \ll 1$) leading to modulational instability of all states with $K(k_0 - K) \neq 0$ at small amplitude. A separate calculation, also near onset ($|u_0| \ll 1$), shows that the TW are initially stable with respect to amplitude perturbations; as usual, this is a consequence of the supercriticality of the primary bifurcation to the TW states.

III. DEFECTS

When a numerical simulation is initialized with small amplitude noise (e.g., of magnitude $\approx 10^{-4}$) superposed on the nonzero homogeneous solution (2)–(3) or the TW solution (8)–(9) the solutions generally evolve into different TWs that travel in opposite directions in different locations. When this is the case in a periodic domain an even number of defects is created within the domain. In one dimension there are two

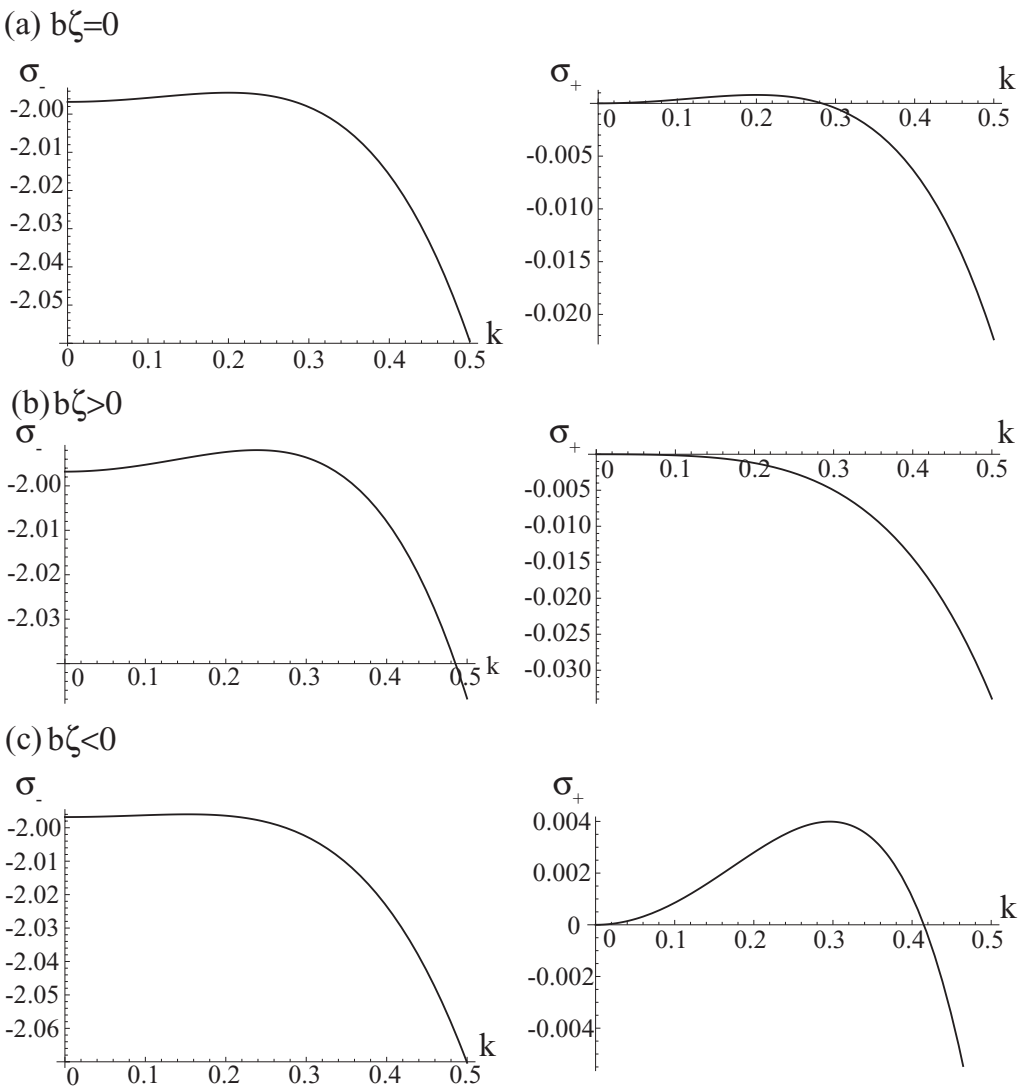

FIG. 1. The growth rates $\sigma_\pm$ of infinitesimal perturbations of the nontrivial homogeneous solution (2)–(3) as functions of the wave number k. Only σ_+ leads to an instability. Parameters: $r = 1$, $b = -0.5$, $k_0 = 0.2$, $\beta = 1$, and $\zeta = 0, -0.1, 0.1$ in (a)–(c), respectively. The long-wavelength instability is suppressed for $b\zeta > 0$ (b) or enhanced for $b\zeta < 0$ (c).

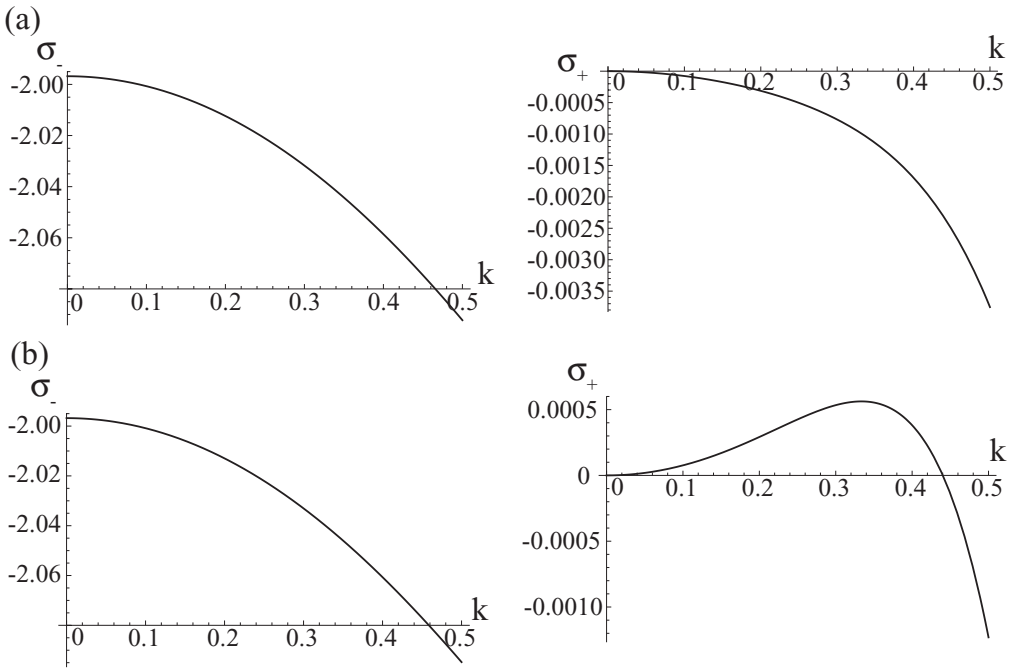

FIG. 2. Stability analysis of the TW solution (8)–(9). Parameters: $r = 1$, $b = -1$, $K = k_0 = 0.2$, $\zeta = 0$, and (a) $\beta = 0.9$ and (b) $\beta = 1.1$. When $K = k_0$ and $\zeta = 0$ there exists a long-wavelength instability for $1 + b\beta < 0$.

types of defects, sources and sinks. The source, as the name suggests, acts as a source of waves, while a sink arises at locations where oppositely traveling waves collide. Figure 3 shows a typical example of such defects in the CSHE. Much is known about the properties of these defects, mostly gleaned from studies of defects in the CCGLEs [26,33]. Reference [37] provides a general classification of defects in oscillatory media. Related structures, called domain walls, connecting homogeneous states with constant but opposite phase have been widely studied in optics, in both one [43] and two [44–46] dimensions.

A. Onset of absolute instability

A source serves to select the wave number of the waves emitted from it. This wave number is determined from the nonlinear dispersion relation by the frequency of the waves emitted from the core. When the core is broad (i.e., the amplitude of the solution is small over a broad region) the frequency selected is the frequency of infinitesimal waves. These obey the dispersion relation

$$i\sigma = r - i\zeta k^2 - (1 + i\beta)\left(k_0^2 - k^2\right)^2, \tag{14}$$

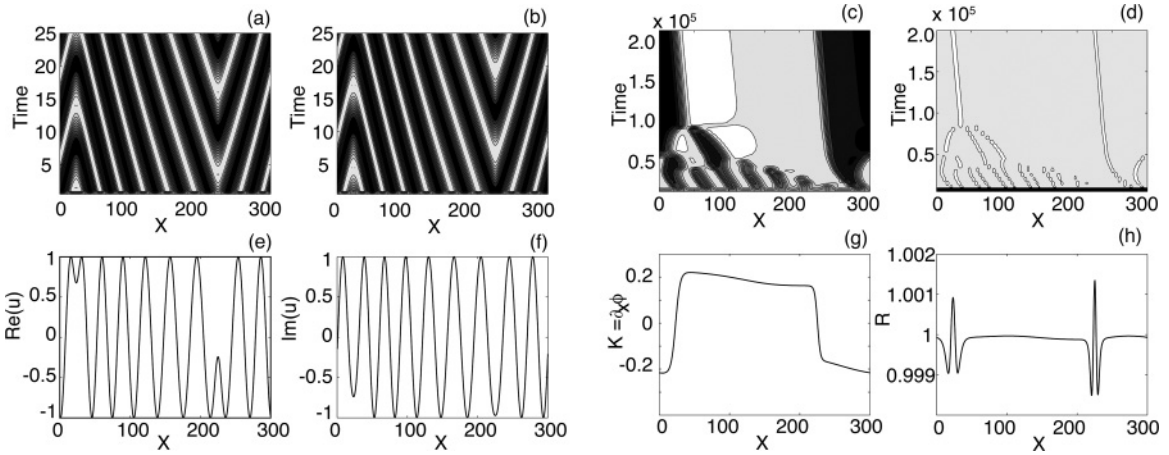

FIG. 3. Temporal simulation of the CSHE with complex coefficients starting from a TW with wave number $K_0 = 0.063$ and superposed small amplitude noise. (a)–(d) Space-time plots of the time evolution of Reu, Imu, the local wave number $K \equiv \phi_x$, and the amplitude R, respectively. Panels (a) and (b) show the last 25 time steps of the much longer simulation shown in panels (c) and (d) that show the details of the slow coarsening process ultimately resulting in a single source and a single sink. White/black regions correspond to high/low values of K or R. (e)–(h) The profiles at the last time step of (a)–(d). Parameters: $r = 1$, $b = -0.5$ and $k_0 = 0.2$, $L = 300$, $N = 1024$ (parameters not mentioned are zero).

where $\sigma \equiv \lambda + i\omega$ and k is the perturbation wave number. These waves set in at $r = 0$ with $k = k_0$, and for $r > 0$ waves with $(k_0^2 - k^2)^2 < r$ have a positive growth rate λ and frequency $\omega = -\zeta k^2 - \beta(k_0^2 - k^2)^2$. Using these results we can define the phase speed $c_p = \omega/k$ and the group speed $c_g = \partial\omega/\partial k$. The phase speed c_p is in general large compared to c_g (this is certainly the case when k is small). This is also clear from the solution shown in Fig. 3 where the drift velocity of the defects $v \approx -10^{-4}$ [see panels (c) and (d)] is small compared to the phase speed c_p of the TW [$|c_p| = \omega/|K| \approx 2.5$, $\omega \approx 0.5$, $K \approx \pm k_0 = 0.2$, see panels (a) and (b)]. Because of this large difference in speed the oscillatory instability is *convective* at onset. Sources can be present only when the instability becomes *absolute* so that the traveling perturbations grow faster than they propagate. The computation of the threshold for absolute instability follows standard procedure [26,34,47]. Using Eq. (14), where $k \equiv k_R + ik_I$, and seeking the location in the complex k plane where $c_g = 0$, one finds

$$i\zeta = 2(1 + i\beta)\left(k_0^2 - k^2\right). \tag{15}$$

Equation (15) together with Eq. (14) represent four equations which determine k_R, k_I, the threshold value $r = r_a$, and the corresponding frequency $\omega = \omega_a$. It is this frequency that in turn determines the wave number of the nonlinear waves emitted by the source. This wave number will in general differ from the wave number k_R selected at $r = r_a$. We obtain

$$r_a = \frac{\zeta^2}{4(1+\beta^2)}, \quad \omega_a = -\zeta k_0^2 + \frac{\zeta^2\beta}{4(1+\beta^2)}, \tag{16}$$

together with the equations

$$k_0^2 - k_R^2 + k_I^2 = \rho, \quad k_R k_I = -\frac{\rho}{2\beta}, \tag{17}$$

where

$$\rho \equiv \frac{1}{2}\left(\frac{\beta\zeta}{1+\beta^2}\right). \tag{18}$$

Thus,

$$\begin{aligned} k_R^2 &= \tfrac{1}{2}\left(k_0^2 - \rho + \sqrt{\left(k_0^2 - \rho\right)^2 + \rho^2/\beta^2}\right), \\ k_I^2 &= \tfrac{1}{2}\left(\rho - k_0^2 + \sqrt{\left(k_0^2 - \rho\right)^2 + \rho^2/\beta^2}\right), \end{aligned} \tag{19}$$

and the profile of the source at $x = 0$ is exponential at small amplitude and given by $|u| \sim \exp(\pm k_I x)$. Note that k_R is nonzero, in contrast to the CCGLE case studied in Ref. [47]. In particular, when $\zeta = 0$ we have $|k_R| = |k_I| = k_0$; when $\zeta \neq 0$ and $k_0^2 = \rho > 0$ we have $|k_R| = |k_I| = \sqrt{|\rho/2\beta|}$.

The above analysis suggests that when $r > r_a$ stationary sources are present and that these select the frequency ω_a when $r \approx r_a$; this frequency in turn selects the wave number K of the emitted waves in the far field according to

$$\omega_a = -br_a + (b - \beta)\left(k_0^2 - k^2\right)^2 - \zeta K^2. \tag{20}$$

With increasing r these symmetric sources may lose stability in different ways. This loss of stability may arise via a parity-breaking bifurcation leading to a drifting defect emitting waves with different wave numbers fore and aft, or via a Hopf bifurcation leading to a pulsating source. A reflection symmetry-breaking Hopf bifurcation is also possible [48]; this leads to a one-dimensional spiral wave, where the source drifts first in one direction and then in the opposite direction, resulting in a zigzag space-time trajectory.

On the other hand, when $r < r_a$ no stationary sources are expected although stationary sinks may remain. Sinks are, in general, much more robust since they form as a result of a collision of waves, and these cannot be perturbed away [26,47]. Their structure is determined locally by the amplitude, frequencies, and wave numbers of the incoming wave trains, and these are, in turn, determined by the sources. If the incoming waves have different frequencies and wave numbers the sink may drift. If the incoming waves are Benjamin-Feir unstable, the sink may undergo irregular back-and-forth oscillations [26,47]. Thus, both sources and sinks can undergo complex dynamical behavior. However, we expect that in the regime $0 < r < r_a$, present provided $\zeta \neq 0$, time-dependent sources may remain, just as in the CCGLE case, coexisting with either stationary or nonstationary sinks, depending on the properties of the waves emitted by the sources.

An example of the destabilization of the source as r is reduced below $r_a \approx 0.125$ is shown in Fig. 4. Figures 4(a) and 4(b) are computed with $k_0 = 0.2$ starting from an initial condition consisting of two TW with wave numbers $\pm k_0$ each occupying a region of width $L/2$. The simulations show, in agreement with theory, that for $r < r_a$, a time-dependent solution is present, while for $r > r_a$ a time-independent structure is the long-time attractor of the system. This solution resembles states described by the convective Cahn-Hilliard equation, as discussed further in Sec. VI A. In contrast, for $k_0 = 1$, for which the Cahn-Hilliard equation no longer applies, no time-dependent sources are found for $r < r_a$, and the system instead evolves to a single TW (not shown). However, as shown in Fig. 4(c), when $r > r_a$ stable sources are recovered.

B. Onset of convective instability and the CCGLE description

In order to compare our results with those of [26] on the CCGLEs we derive here the CCGLEs from the CSHE. Such a derivation requires a judicious scaling of the parameters and the dependent variable, as appropriate for a computation near the threshold for *convective* instability. We write $r = r_0 + \epsilon^2 r_2, \zeta = \epsilon\hat{\zeta}$, and introduce the slow time $T = \epsilon^2 t$ and the slow spatial scale $X = \epsilon x$. Here $\epsilon \ll 1$ is a small parameter whose magnitude may be defined by setting $r_2 = 1$. As a result the calculation that follows is restricted to a small neighborhood of $r = r_0$, where r_0 is determined below. In this neighborhood we expect the solution u to be small and hence write $u(x,t,\epsilon) = \epsilon u_0(x,X,t,T) + \epsilon^3 u_2(x,X,t,T) + \cdots$. No term of the form $\epsilon^2 u_1(x,X,t,T)$ appears in the expansion owing to the symmetry of CSHE with respect to $u \to -u$. The remaining parameters k_0, b, and β are all treated as $O(1)$ quantities. These scalings capture the expected balance between forcing via the term $(r - r_0)u$, advection at the group velocity, weak dispersion and weak nonlinearity, all of which enter at $O(\epsilon^3)$ in the theory that follows. As mentioned below, this is not the case for other possible scalings of $r - r_0$, ζ, and the dependent variable u, and such regimes are described by evolution equations that differ from the classical CCGLE description.

We seek to describe the evolution of the leading order solution $u_0(x,X,t,T)$ over long times [$T = O(1)$, equivalently $t \sim \epsilon^{-2}$] and large scales [$X = O(1)$, equivalently $x \sim \epsilon^{-1}$].

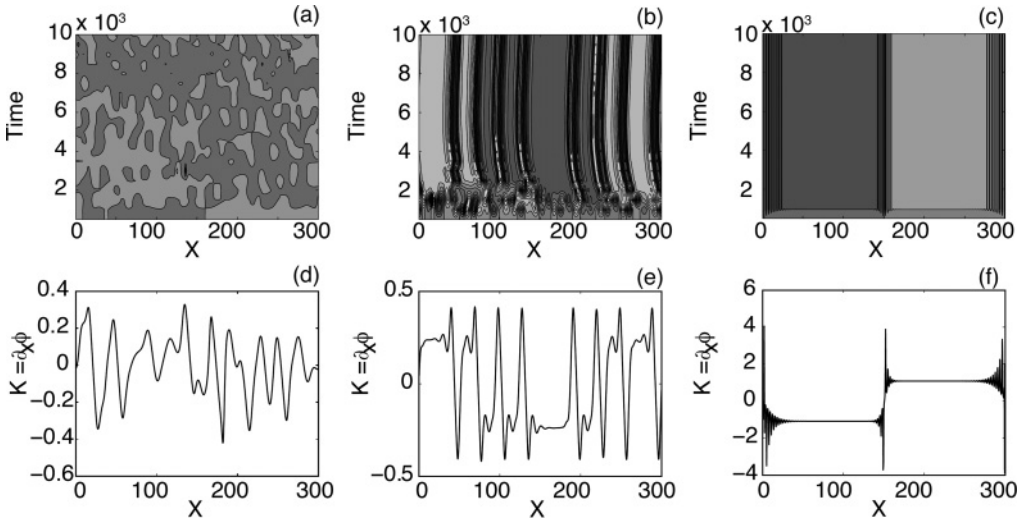

FIG. 4. Temporal simulation of the CSHE with complex coefficients. (a)–(c) Space-time plots of the time evolution of the local wave number K. (d)–(f) The profiles $K(x)$ at the last time step of (a)–(c). White/black regions correspond to high/low values of K. Parameters: $b=-0.5$, $\beta=-1$, $\zeta=-1$, $L=300$, $N=1024$, $r_a=0.125$. (a) $k_0=0.2$, $r=0.1<r_a$. (b) $k_0=0.2$, $r=0.3>r_a$. (c) $k_0=1$, $r=0.3>r_a$.

At $O(\epsilon)$ we obtain

$$u_{0t}=r_0u_0-(1+i\beta)\left(k_0^2+\partial_x^2\right)^2u_0. \tag{21}$$

This equation is solved by

$$u_0=A_L(X,T)\exp(i\omega_0t+ikx)+A_R(X,T)\exp(i\omega_0t-ikx), \tag{22}$$

representing a superposition of left- and right-traveling waves with slowly varying amplitudes $A_L(X,T)$ and $A_R(X,T)$, respectively. Substitution of this expression into Eq. (21) yields the dispersion relation

$$i\omega_0=r_0-(1+i\beta)\left(k_0^2-k^2\right)^2. \tag{23}$$

Thus,

$$r_0=\left(k_0^2-k^2\right)^2,\quad \omega_0=\beta\left(k_0^2-k^2\right)^2. \tag{24}$$

Hence, the onset wave number is given by $k=k_0$, that is, the gravest mode has wave number equal to the intrinsic wave number k_0, and we have $r_0=\omega_0=0$. This is as expected since we have taken r to be real, thereby eliminating the leading order frequency. The value $r_0=0$ corresponds to the threshold for convective instability, and indeed $r_0<r_a$ provided $\zeta\neq0$. Note also that $\omega_0=0$, while at the absolute instability threshold $\omega_a\neq0$.

The CSHE is identically satisfied at $O(\epsilon^2)$, while at $O(\epsilon^3)$ we obtain

$$\begin{aligned}&u_{2t}-r_0u_2+(1+i\beta)\left(k_0^2+\partial_x^2\right)^2u_2\\&\quad=-u_{0T}+r_2u_0+2i\hat{\zeta}u_{0xX}-(1+i\beta)\left[2\left(k_0^2+\partial_x^2\right)u_{0XX}\right.\\&\qquad\left.+4u_{0xxXX}\right]-(1+ib)|u_0|^2u_0.\end{aligned} \tag{25}$$

Since both components of the general solution (22) are in the kernel of the linear operator on the left side of Eq. (25) there are two solvability conditions for this equation:

$$\begin{aligned}A_{L,T}-c_0A_{L,X}&=r_2A_L+4k_0^2(1+i\beta)A_{L,XX}\\&\quad-(1+ib)(|A_L|^2+|A_R|^2)A_L,\end{aligned} \tag{26}$$

$$\begin{aligned}A_{R,T}+c_0A_{R,X}&=r_2A_R+4k_0^2(1+i\beta)A_{R,XX}\\&\quad-(1+ib)(|A_R|^2+|A_L|^2)A_R,\end{aligned} \tag{27}$$

where $c_0=-2\hat{\zeta}k_0$ is the group velocity. After rescaling space and time, these equations form a special case of the equations studied in Ref. [26], viz.,

$$\begin{aligned}A_{L,T}-s_0A_{L,X}&=r_2A_L+(1+ic_1)A_{L,XX}\\&\quad-(1-ic_3)|A_L|^2A_L-g_2(1-ic_2)|A_R|^2A_L,\end{aligned} \tag{28}$$

$$\begin{aligned}A_{R,T}+s_0A_{R,X}&=r_2A_R+(1+ic_1)A_{R,XX}\\&\quad-(1-ic_3)|A_R|^2A_R-g_2(1-ic_2)|A_L|^2A_R,\end{aligned} \tag{29}$$

with $s_0=-\hat{\zeta}$, $c_1=\beta$, $c_2=c_3=-b$, $g_2=1$. In contrast, when $\zeta=O(1)$, $r=O(\epsilon^2)$ one obtains instead the nonlocal CCGLEs derived in Ref. [49], while with $\zeta=O(1)$, $r=O(\epsilon)$ one obtains the hyperbolic equations derived in Refs. [50,51]. The relation between the properties of the local and nonlocal CCGLEs is explored in Refs. [49,52,53]. When $\hat{\zeta}=0$ the above equations reduce to a special case of those studied in Ref. [54], with $\gamma=1$ in their notation. As shown in Ref. [54] (see also Ref. [26]), this parameter value falls near the transition from spatiotemporal intermittency to a steady state with domains of $(A_L,A_R)=(A_L,0)$ and $(A_L,A_R)=(0,A_R)$ separated by domain walls. When $\hat{\zeta}=O(1)$ or equivalently $\zeta=O(\epsilon)$ the critical value of the parameter r_2 at which the source width diverges identified in Refs. [26,34], viz., $r_2=s_0^2/4(1+c_1^2)$, agrees with the more general expression (16a).

We mention that the CCGLEs (28) and (29) contain two extra parameters as compared with Eq. (1), assuming that the parameter k_0 is fixed. Consequently, the behavior exhibited by Eq. (1) is expected to fall between that of a single CGLE and that exhibited by general CCGLEs. In particular, some aspects of the mutual suppression of left-TWs by right-TWs and vice versa may be expected in the dynamics but mutual excitation should be absent.

IV. NUMERICAL EXPLORATION

From studies of the supercritical CSHE with real coefficients [30][1] we know that the intrinsic wave number plays an important role in the observed dynamics. In particular, for small k_0 the system exhibits coarsening behavior with the number of defects gradually decreasing over the course of time and a corresponding increase in the size of the defect-free domains in between. This evolution is described by the Cahn-Hilliard equation for the phase gradient that can be derived from the CSHE on the assumption that this gradient is small. On the other hand, for larger k_0 the system evolves via phase slips and any coarsening that may take place initially is arrested by the formation of bound states of (stationary) defects [30]. We explore here the corresponding behavior when the coefficients in the CSHE are complex and the defects move.

A. Dynamics in the CSHE with a large intrinsic length scale (k_0 small)

1. $b \neq 0, \beta = \zeta = 0$

We start our numerical exploration with the regime in which coarsening is observed in the CSHE with real coefficients assuming that $b \neq 0$, $\beta = \zeta = 0$, and scan the dynamical behavior as the coefficient b becomes more and more negative. Figure 3 shows a numerical simulation of the time evolution in the CSHE with periodic boundary conditions and $r = 1$, $b = -0.5$, and $k_0 = 0.2$ with the remaining parameters zero. Here and in the remainder of this section small amplitude random noise superposed on the nonzero homogeneous solution (2)–(3) is taken as the initial condition. The figure shows that the final state of the system consists of one source and one sink separating two counterpropagating TWs [see Figs. 3(e) and 3(f)]. This situation corresponds to a pair of connections or fronts between a positive and a negative phase gradient $K \equiv \phi_x$, thereby forming a pair of localized structures (LSs); this structure manifests itself in the amplitude as well [see Figs. 3(g) and 3(h)]. The source and sink are distinguished by the asymptotic phase speed far from the LS: If this speed is outward the defect corresponds to a source; if it is inward the defect is a sink [see Figs. 3(a) and 3(b)]. The source is an active coherent structure that sends out waves in both directions, while the sink is sandwiched between TWs whose phase velocity points inward. It is clear from Fig. 3 that initially several LSs form and that these annihilate pairwise leaving only a single sink and a single source which form a slowly drifting bound state (drift speed $v \approx -10^{-4}$). Similar coarsening behavior is observed for less negative values of b as well, and is described by a Cahn-Hilliard type equation derived in Sec. V.

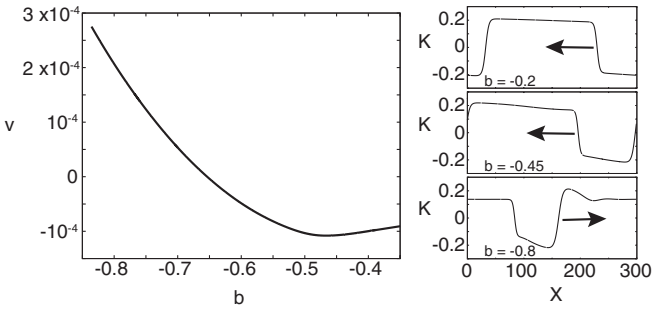

FIG. 5. The velocity of a front in the derivative of the phase (a shocklike structure in the local wave number $K \equiv \phi_x$) as a function of the parameter b obtained by numerical continuation of the solution in Figs. 3(g) and 3(h) for a fixed spatial average of K ($\bar{K} = 0.063$). Other parameters are as in Fig. 3. The right panels show the resulting K profiles for three different values of b.

The drift velocity v of the bound state in Fig. 3 is nonzero because of the presence of an asymmetry between left- and right-TWs. This asymmetry is quantified by the spatial average of the wave number K, here $\bar{K} = 0.063$, which remains constant. The results of numerical continuation shown in Fig. 5 reveal that the drift speed depends on the parameter b and does so in a nonmonotonic fashion, largely because of changes in the width of this state. For the solution in Figs. 3(g) and 3(h) ($b = -0.5$) the drift velocity $v \approx -10^{-4}$ and is small compared to the phase speed c_p of the waves ($|c_p| = \omega/|K| \approx 2.5$, $\omega \approx 0.5$, $K \approx \pm k_0 = 0.2$). As b decreases from $b = 0$, the (leftward) drift velocity first increases but starts to decrease again when $b \approx -0.5$ and crosses zero when $b \approx -0.67$ and thereafter the bound state drifts toward the right. The solution profiles shown in the right panels in Fig. 5 show that this reversal in the direction of drift is a consequence of an overshoot in the profile that develops with decreasing b.

The change in dynamical behavior when b decreases is exemplified by Fig. 6. When $b = -1$, one observes an initial back-and-forth movement of the phase gradient fronts (and the associated LSs), but after this transient the remaining LSs (a source and a sink) form a stationary bound state [see Figs. 6(a) and 6(b)]. With further decrease in b a regime of spatiotemporal intermittency is encountered [see Figs. 6(c) and 6(d)]. In this regime, defect chaos coexists with TWs. Patches of TWs are separated by various LSs, some of which are created and destroyed in rapid succession, while others persist for a longer period and display the same type of back-and-forth movement, as seen in the transient in Figs. 6(a) and 6(b). Similar spatiotemporal intermittency has been studied in the context of the CGLE [5,26,31,54]. When b is decreased even further, the system exhibits more and more spatiotemporally disordered regimes, whose presence we attribute to modulational instability of the basic TW state.

The coarsening behavior described here involves sources and sinks of counterpropagating TWs, in contrast to earlier studies of coarsening behavior between domain walls in one [43] and two [44–46] dimensions. However, curvature effects that give rise to different types of growth laws in two dimensions [44–46] are absent.

[1]Equation (37) in Ref. [30] should read $\beta_2 = \frac{K_s^2(k_0^2 - 3K_s^2)}{R_s^2} - \frac{1}{2}\beta_1^2$.

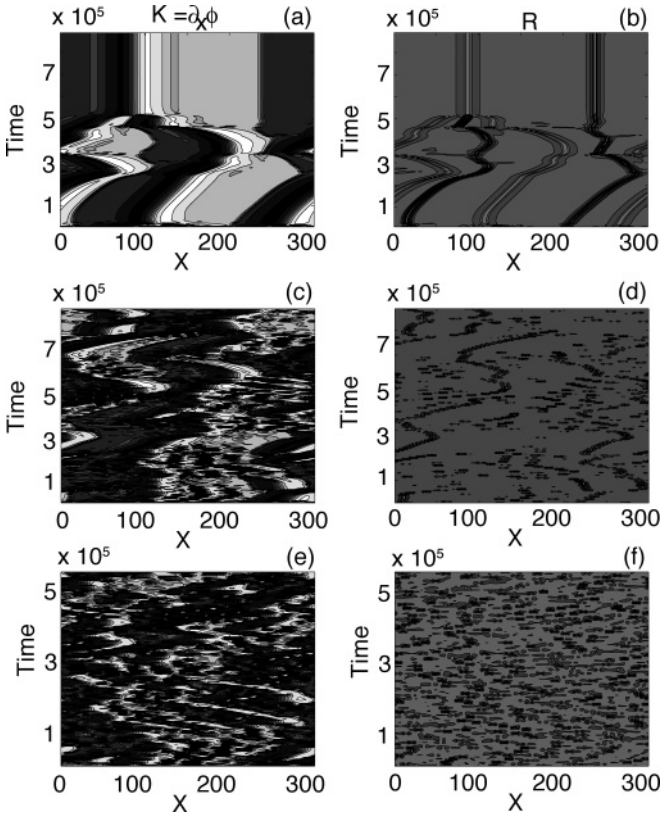

FIG. 6. Temporal simulation of the CSHE with complex coefficients. Space-time plots of the time evolution of the local wave number $K \equiv \phi_x$ [(a), (c), (e)] and the amplitude R [(b), (d), (f)] for increasing values of $|b|$. White/black regions correspond to high/low values of K or R. Parameters: $r = 1$, $b = -1$ [(a), (b)], $b = -1.5$ [(c), (d)], $b = -2$ [(e), (f)] and $k_0 = 0.2$, $L = 300$, $N = 1024$ (parameters not mentioned are zero).

2. $b \neq 0, \beta \neq 0, \zeta = 0$

Figures 7–9 show the results of numerical simulations when b remains fixed ($b = -1$) and the parameter β is varied instead. Figure 7 shows typical behavior that is observed when $\beta < 0$. For all $\beta < 0$ coarsening dynamics are found, and coarsening proceeds until only one source-sink pair is left in the system. Both the source and the sink are then stable and either remain stationary or slowly drift in time.

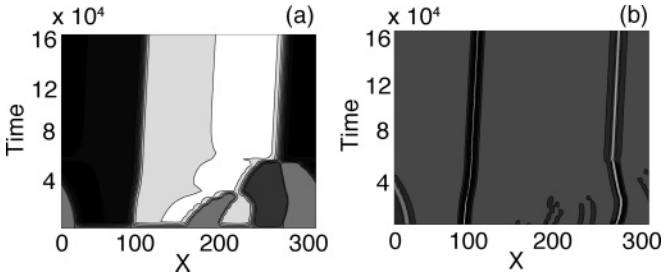

FIG. 7. Temporal simulation of the CSHE with complex coefficients. Space-time plots of the time evolution of (a) the local wave number $K \equiv \phi_x$ and (b) the amplitude R. White/black correspond to high/low values of K or R. Parameters: $r = 1, b = -1, \beta = -2$, and $k_0 = 0.2$, $L = 300$, $N = 1024$ (parameters not mentioned are zero).

When $0 < \beta \lesssim 1$ spatiotemporal intermittency is found. Figure 8, computed for $\beta = 1$ shows typical space-time plots in this regime. The figure reveals a uniformly drifting complex oscillation in the real and imaginary parts of u with the property that $R \approx 1$ throughout the duration of the time series [see Fig. 8(h)]. Thus, the oscillation shown is associated with phase variation and not amplitude variation. However, for larger β the behavior changes qualitatively and for $\beta \gtrsim 1$ drifting TW-like states are no longer found in numerical simulations. With random initial conditions, the system evolves to a state which oscillates with wave number comparable to k_0 in both the phase gradient $K = \phi_x$ and the amplitude R, while slowly drifting. A state of this type is shown in Figs. 9(a) and 9(b), which reveal that the spatial oscillations are likely quasiperiodic, with a longer wavelength modulation superposed on the $2\pi/k_0$ wavelength. This modulation becomes more and more pronounced as β increases. We can see, for example, in Figs. 9(c) and 9(d), that an increase in β leads to an increase of the local wave number K and the creation and destruction of defects resulting in spatiotemporal chaos. Such perturbations of the basic state [panels (a) and (b)] arise spontaneously, indicating the presence of a linear instability. The dynamics evolve on faster time scales and no coherent structures can be observed. Similar behavior is also observed in the CGLE [5,26]. In the case of the CGLE, this spatiotemporal chaos has been described using the Kuramoto-Sivashinsky equation [31]. We show in Sec. V that this is so also in the present case.

B. Dynamics in the CSHE with a larger intrinsic length scale [$k_0 = O(1)$]

In previous work on the CSHE with real coefficients [30,55] we have shown that coarsening terminates when the intrinsic wave number k_0 is larger, and characterized the transition from coarsening dynamics to the frozen state that results. The frozen state consists of bound pairs of defects locked together via their oscillatory tails, and the crossover transition can be accurately attributed to the first appearance of these tails.

In this section, we numerically explore the dynamical behavior that arises in the CSHE with complex coefficients when $k_0 = 1$, a value large enough for oscillatory tails to exist. As before, we first consider the case $\beta = 0$ and then allow both b and β to have nonzero values.

1. $b \neq 0, \beta = \zeta = 0$

The results for $\beta = \zeta = 0$ and small negative values of b are shown in Fig. 10. Starting from random initial conditions, the system relaxes after a brief transient behavior to a bound state of two breathing LSs which drifts to the left at a constant speed. In contrast to the case of small k_0, more than one drifting source and sink pair can be present in the system as long-time coarsening no longer takes place. The constituents of these bound states are typically unsteady, exhibiting small amplitude oscillations that may be periodic or chaotic. Moreover, Fig. 10 also reveals that the wave number within the bound state is no longer constant and instead varies linearly with the position x within the structure. This type of behavior is characteristic of

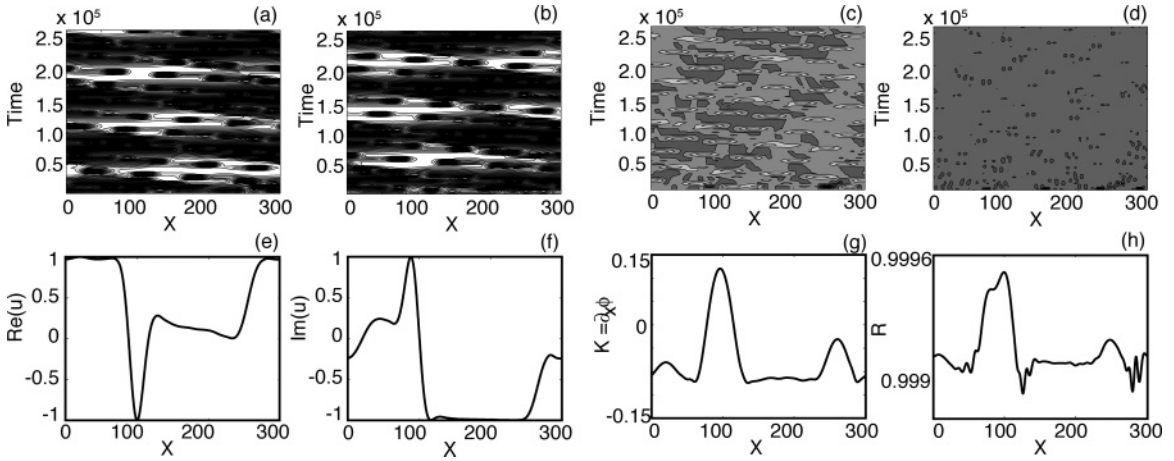

FIG. 8. Temporal simulation of the CSHE with complex coefficients. Space-time plots of the time evolution of (a) Reu, (b) Imu, (c) the local wave number $K \equiv \phi_x$, and (d) the amplitude $R \equiv |u|$. (e)–(h) The profiles at the last time step of (a)–(d). White/black regions correspond to high/low values of K or R. Parameters: $r = 1$, $b = -1$, $\beta = 1$, and $k_0 = 0.2$, $L = 300$, $N = 1024$ (parameters not mentioned are zero).

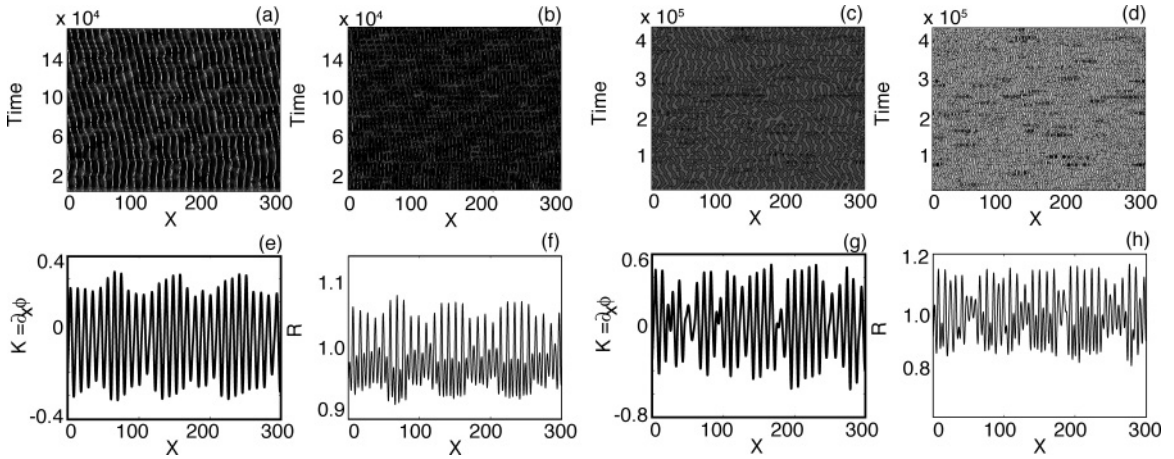

FIG. 9. Temporal simulation of the CSHE with complex coefficients. Space-time plots of the time evolution of (a), (c) the local wave number $K \equiv \phi_x$ and (b), (d) the amplitude R. (e)–(h) The profiles at the last time step of (a)–(d). White/black regions correspond to high/low values of K or R. Parameters: $r = 1$, $b = -1$, $\beta = 2$ (a), (b), (e), (f), $\beta = 3$ (c), (d), (g), (h), and $k_0 = 0.2$, $L = 300$, $N = 1024$ (parameters not mentioned are zero).

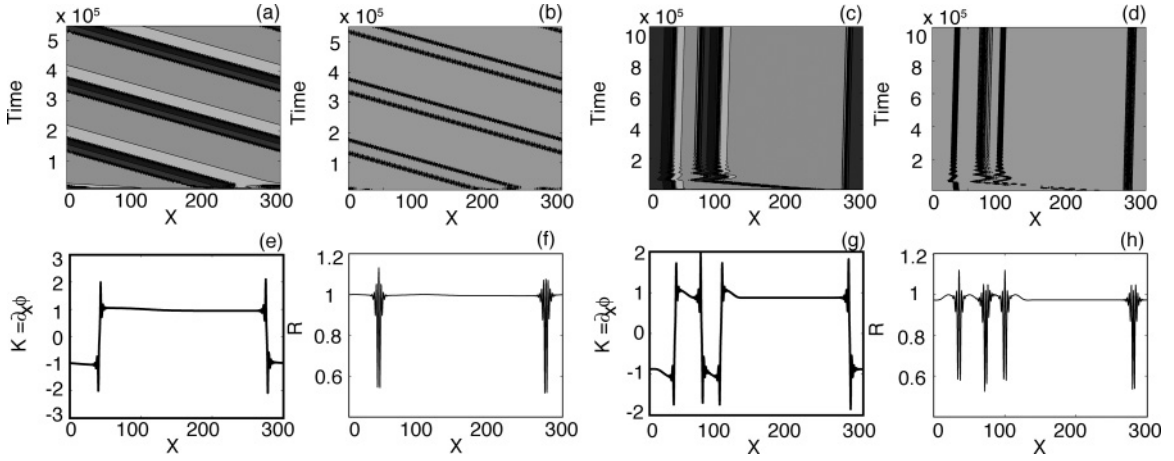

FIG. 10. Temporal simulation of the CSHE with complex coefficients. Space-time plots of the time evolution of (a), (c) the local wave number $K \equiv \phi_x$ and (b), (d) the amplitude R. (e)–(h) The profiles at the last time step of (a)–(d). White/black regions correspond to high/low values of K or R. Parameters: $r = 1$, $b = -0.5$ (a), (b), (e), (f), $b = -1$ (c), (d), (g), (h), and $k_0 = 1$, $L = 300$, $N = 1024$ (parameters not mentioned are zero).

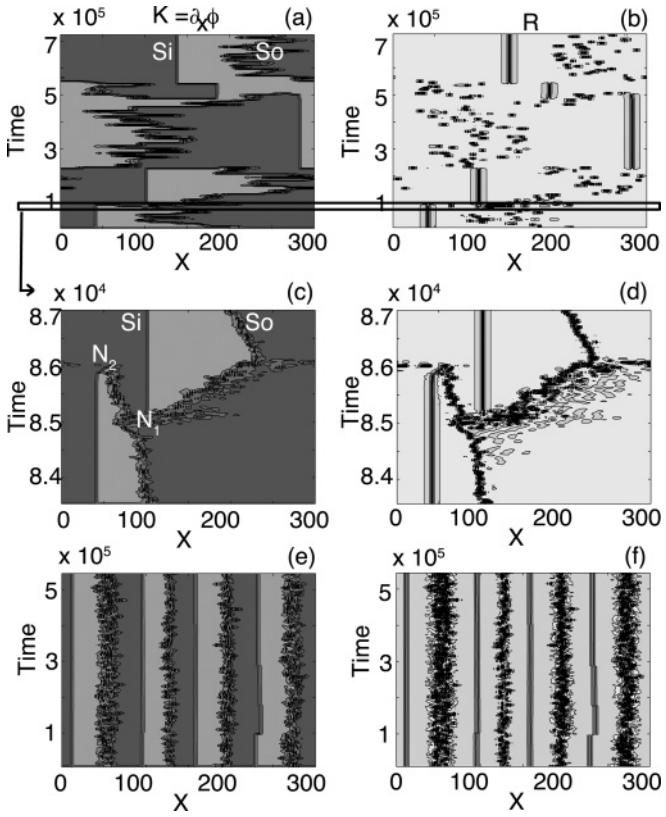

FIG. 11. Temporal simulation of the CSHE with complex coefficients. Space-time plots of the time evolution of the local wave number $K \equiv \phi_x$ [(a), (c), (e)] and the amplitude R [(b), (d), (f)], for decreasing values of b. Panels (c) and (d) represent a zoom of the black box in (a) and (b). White/black regions correspond to high/low values of K or R. Sinks (Si) are stationary and stable for long time intervals, while sources (So) oscillate wildly. Nucleation points creating or destroying a source/sink pair are denoted by N_1, N_2. Parameters: $r = 1$, $b = -3$ (a)–(d) and $b = -5$ (e) and (f), and $k_0 = 1$, $L = 300$, $N = 1024$ (parameters not mentioned are zero).

systems described by a Burger's type equation, as discussed further in Sec. VI.

Figure 11 shows spatiotemporal chaotic regimes that are found when b is more negative. Instead of drifting LSs, one observes a stable stationary sink solution Si, while the source So undergoes apparently chaotic oscillations. This behavior is reminiscent of the source-induced bimodal chaos that is observed in CCGLEs [26], although in the latter case the sink slowly drifts. However, the bimodal chaos is only observed in CCGLEs and is not present in a single CGLE. While the sink remains stationary and stable over long periods of time, one can see in Figs. 11(a) and 11(b) that at certain points in time the sink Si is abruptly destroyed and recreated elsewhere in space ($b = -3$ in this case). Panels (c) and (d) show a magnification of such an event [indicated by the black box in Figs. 11(a) and 11(b)]. The magnification shows that a new stable sink/chaotic source pair nucleates at point N_1 first and does so via the original chaotic source; soon after this occurs the original sink and chaotic source annihilate one another in point N_2. Thus, after this process is completed only one stable sink/chaotic source pair is again present in the system, but at a different location than before. This behavior repeats intermittently in time. To the best of our knowledge, such behavior has not been observed in other systems.

Further decrease in b leads to multiple stable sink/chaotic source pairs within the domain as illustrated in Figs. 11(e) and 11(f) for $b = -5$. For this parameter value nucleation of new sink/source pairs (and subsequent annihilation) is apparently absent and the observed dynamic structure persists indefinitely, much as in the CCGLEs [26].

Qualitatively the same behavior is observed for positive values of b as well. For small values of b, single or multiple drifting source/sink pairs are observed, while increasing b eventually leads to the creation of one stable sink/chaotic source pair (e.g., for $b = 3$). For yet higher values of b, multiple coexisting stable sink/chaotic source pairs are again found (e.g., for $b = 5$).

2. $b \neq 0, \beta \neq 0, \zeta = 0$

Figure 12 shows the dynamics that are observed when $\beta \neq 0$. Since a complete characterization of the spatiotemporal dynamics in the (b,β) parameter space is beyond the scope of this work we limit ourselves to analyzing the dynamical behavior along the $b = -1$ slice through this space, scanning β from -5 to 5. The following behavior is observed.[2]

(i) For $\beta < -3.4$, the whole space is filled with coexisting stationary source/sink pairs. For the chosen domain width $L = 300$, either three or four pairs are present in the system [see, e.g., Fig. 12(a); $\beta = -5$].

(ii) In the region $-3.4 < \beta < -2.5$, the same source-sink pairs still coexist, but are no longer stationary and exhibit slight "breathing" (time-periodic) behavior [see, e.g., Fig. 12(b); $\beta = -3$].

(iii) When β increases within the interval $-2.5 < \beta < 1.2$, the number of source/sink pairs in the system tends to diminish. Furthermore, on top of the "breathing" behavior, the sources and sinks start to drift [see, e.g., Figs. 12(c) and 12(d); $\beta = -2.5$ and $\beta = 1$]. We remark that around $\beta \approx -0.1$ the drift speed of the structures becomes very slow.

(iv) For $1.2 < \beta < 4$, both source and sink are again stabilized and remain stationary [see, e.g., Fig. 12(e); $\beta = 3$].

(v) In the interval $4 < \beta < 4.2$, time-periodic "breathing" behavior is again observed, but with time-periodic oscillations that are much more pronounced than in the previous cases. Moreover, only the source shows time-periodic behavior, while the sink remains stationary and stable [see, e.g., Fig. 12(f); $\beta = 4.1$].

(vi) When increasing β in the interval $4.2 < \beta < 4.8$, the time-periodicity of the source is lost and is replaced by chaotic

[2]We remark that the boundaries mentioned in this classification of dynamical behavior have been numerically determined with an accuracy of $\Delta\beta = 0.1$.

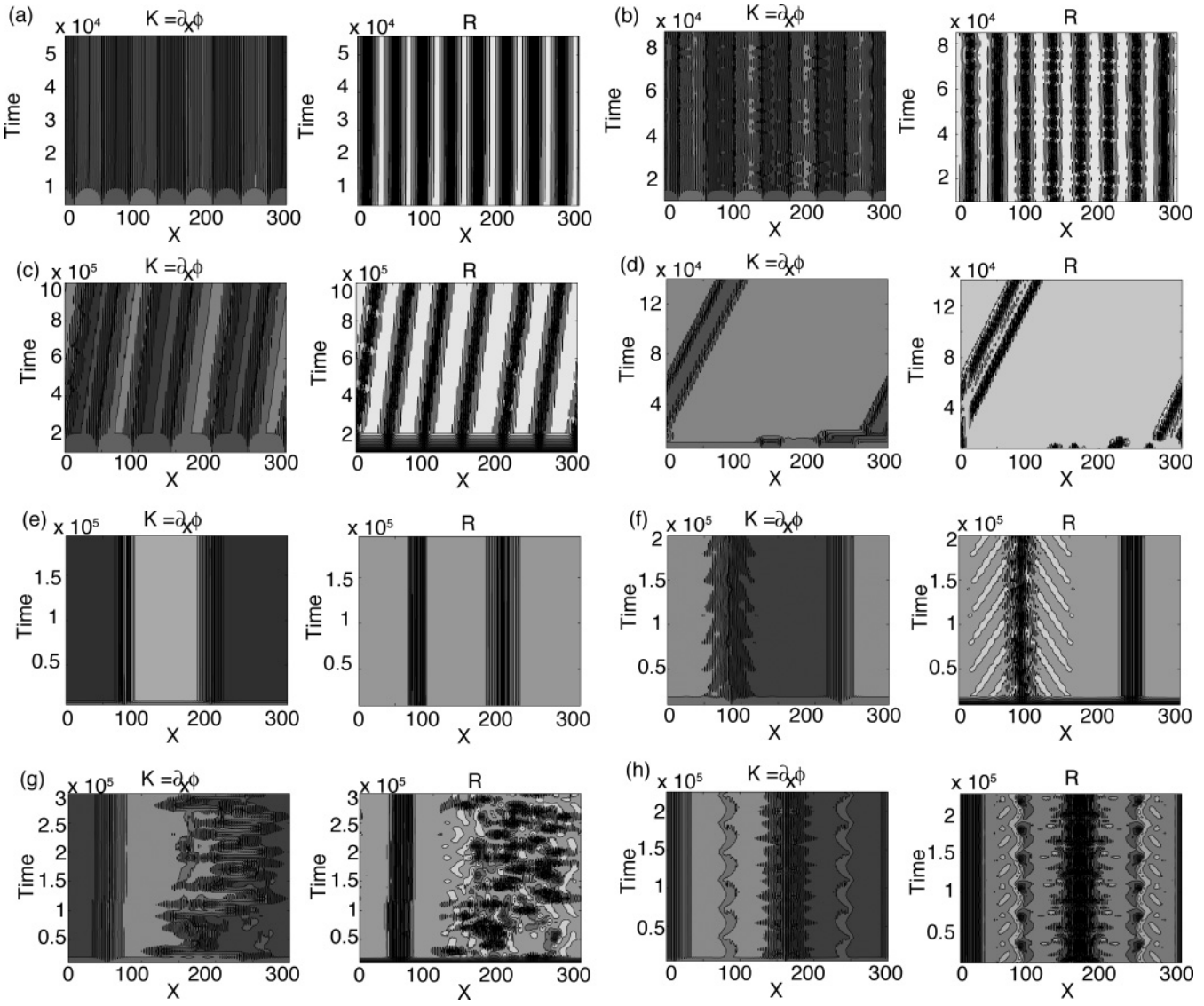

FIG. 12. Temporal simulation of the CSHE with complex coefficients in terms of space-time plots showing the time evolution of the local wave number $K \equiv \phi_x$ and the amplitude R. White/black regions correspond to high/low values of K or R. Parameters: $r = 1$, $b = -1$, $\beta = -5$, (a) -3, (b) -2.5, (c) 1, (d) 3, (e) 4.1, (f) 4.5, (g) and 5, (h) $k_0 = 1$, $L = 300$, $N = 1024$ (parameters not mentioned are zero).

behavior; the sink remains stable and more or less stationary [see, e.g., Fig. 12(g); $\beta = 4.5$].

(vii) Finally, for $\beta > 4.8$, the source is again only mildly chaotic but additional time-dependent substructures appear in the middle of each TW domain that oscillate in phase with the source [see, e.g., Fig. 12(h); $\beta = 5$].

Stable breathing sinks similar to Fig. 12(f) have recently been computed in doubly diffusive convection [56].

In the next section, we derive a nonlinear phase equation modeling the evolution of long-wavelength perturbations of the homogeneous amplitude solutions. This phase equation will prove useful for interpreting some of the numerically observed dynamics.

V. NONLINEAR PHASE EQUATIONS

Large length scale perturbations of the phase of a wave evolve on a slow time scale relative to perturbations of the amplitude. This fact allows us to decouple the amplitude perturbations from those of the phase, through a procedure analogous to center manifold reduction, a reduction procedure employed in studies of finite-dimensional dynamical systems. The equation that results is an equation for the slow evolution of ϕ, the wave phase, or, equivalently, for the wave number $K \equiv \partial_x \phi$. We consider two cases, the first being the evolution of spatial perturbations of the homogeneous oscillations in time ($|K| \ll 1$) and the second studying perturbations of a TW [$K = O(1)$].

We begin by rewriting the CSHE in terms of the amplitude R and the phase gradient $K \equiv \partial_x \phi$, where $u(x,t) \equiv R(x,t) \exp i\phi(x,t)$. Thus,

$$R_t = rR - R^3 - k_0^4 R + \left[-2k_0^2 R_{xx} + 6K^2 R_{xx} + 12K R_x K_x - RK^4 + 2RK^2 k_0^2 + 3RK_x^2 + 4KK_{xx}R - R_{xxxx}\right] + \beta\left[-4K^3 R_x + 6K_x R_{xx} + 4R_x K_{xx} + 4KR_x k_0^2 + 4KR_{xxx} - 6RK^2 K_x + 2Rk_0^2 K_x + RK_{xxx}\right] - \zeta[2R_x K + RK_x], \quad (30)$$

$$K_t = -2bRR_x - \left[4\frac{R_{xxx}}{R}K + 6\frac{R_{xx}}{R}K_x + 4\frac{R_x}{R}K_{xx} + K_{xxx} - 4\frac{R_x}{R}K^3 - 6K^2 K_x + 2k_0^2 K_x + 4k_0^2 K\frac{R_x}{R}\right]_x + \beta\left[-2k_0^2\frac{R_{xx}}{R} + 6K^2\frac{R_{xx}}{R} + 12KK_x\frac{R_x}{R} - K^4 + 2k_0^2K^2 + 3K_x^2 + 4KK_{xx} - \frac{R_{xxxx}}{R}\right]_x + \zeta\left[\frac{R_{xx}}{R} - K^2\right]_x. \quad (31)$$

In this formulation the temporal oscillation frequency Ω of the wave train is absent.

Equations (30) and (31) are exact. In the following we consider two distinct cases. In the first we take a finite amplitude spatially homogeneous oscillation, corresponding to $R = R_0$ (a constant) and $K = 0$. We consider wave number perturbations with $K = O(\epsilon)$, where $\epsilon \ll 1$; that is, we consider the evolution of the system from initial conditions that vary slowly in space, on an $O(\epsilon^{-1})$ scale only. In order to balance the evolution on these large scales we need to select the correct size of the perturbation $R = R_0 + u$. Since the basic oscillation is invariant under reflection $x \to -x$ the resulting evolution equation must also respect this symmetry. In the second case, we take $R = R_0$ (a constant) and $K = O(1)$, representing a homogeneous wave train. The balances in this case are different, and since the basic wave train is no longer invariant under $x \to -x$ the resulting evolution equation for wave number perturbations will also be different. In particular, the wave number perturbations are now expected to propagate and at the same time to steepen.

In order to capture transitions between different regimes we do not explicitly scale the variables with ϵ but employ an iterative method that can be checked for consistency at each step. Unless otherwise stated all parameters are treated as $O(1)$ quantities, in contrast to the CCGLE derivation.

A. The $|K| \ll 1$ case

We write the perturbation of a homogeneous oscillation in the form $R = R_0 + u$, $K = v$, where $R_0^2 \equiv r - k_0^4$, and take v to be $O(\epsilon)$, thereby defining the modulation scale ϵ^{-1}. We suppose that the amplitude perturbation u varies on the same scale, and hence take all spatial derivatives to be $O(\epsilon)$. Temporal derivatives are taken to be slow, relative to Ω^{-1}, and will, in fact, be $O(\epsilon^4)$, as can be checked *a posteriori*. The primary balance in Eq. (30) is then provided by

$$u_t = -2R_0^2 u + 2k_0^2 R_0(\beta v_x + v^2) - \zeta R_0 v_x + \text{h.o.t.}, \quad (32)$$

where h.o.t. denotes higher order terms. Since v_x and v^2 are both $O(\epsilon^2)$ we conclude that we must take $u = O(\epsilon^2)$; that is, we link the perturbation amplitude u to the (inverse) scale of the modulation as specified by v. Thus, $R_0 u \approx (k_0^2\beta - \frac{1}{2}\zeta)v_x + k_0^2 v^2$. Substituting this result in Eq. (31) for the phase gradient results in a modified convective Cahn-Hilliard-type equation:

$$v_t = [\gamma v - a v_{xx} - \kappa_0 v^3]_{xx} + \left[\tfrac{1}{2}Dv^2 + cv_x^2 + dv^4 + evv_{xx}\right]_x + \text{h.o.t.} \quad (33)$$

This equation is equivariant with respect to the operation $x \to -x$, $v \to -v$, a symmetry inherited from the fact that $v \equiv \phi_x$, with the phase ϕ a scalar. When the coefficients γ and D are both $O(1)$ the wave number v evolves on an $O(\epsilon^{-2})$ time scale and is of Burger's type at leading order, that is, at $O(\epsilon^3)$. The shock formation that results is regularized by the diffusion coefficient γ provided $\gamma > 0$. However, when $\gamma < 0$ (Benjamin-Feir instability) the diffusion term leads to singularities in finite time and to control these it is necessary to carry the derivation of the phase equation to $O(\epsilon^5)$, resulting in the presence of several additional terms, all of which are included in Eq. (33). These terms become important on an $O(\epsilon^{-4})$ time scale, implying that the above expansion is no longer uniform in time. Of the new terms, those in the first bracket constitute the classical Cahn-Hilliard equation describing coarsening over long time scales. The appearance of this equation in the context of phase evolution goes back to the work of Malomed *et al.* [35] (see also [30,55,57,58]). However, the terms in the second bracket lead to nonlinear steepening resulting in instabilities that arrest and disrupt the slow coarsening process as described for $c = d = e = 0$ in Ref. [59] and in the general case in Sec. VI A. For other choices of the coefficients Eq. (33) resembles the Kuramoto-Sivashinsky equation, and on large domains exhibits spatiotemporal chaos [31]. A discussion of this regime and a comparison of its properties with those of the CSHE is deferred to Sec. VI.

The coefficients in Eq. (33) are given by

$$\gamma = -2k_0^2(1 + b\beta) + b\zeta, \quad (34)$$

$$\kappa_0 = -2\left(1 - \frac{k_0^4}{R_0^2} + \frac{1}{6}\frac{\gamma k_0^2}{R_0^2}\right), \quad (35)$$

$$D = 4k_0^2(\beta - b) - 2\zeta, \quad (36)$$

$$a = 1 + \frac{\left(2k_0^2\beta - \zeta\right)^2}{2R_0^2}, \quad (37)$$

$$c = 3\beta - \frac{b}{4R_0^2}\left(2k_0^2\beta - \zeta\right)^2 - \frac{2k_0^2}{R_0^2}\left(2k_0^2\beta - \zeta\right), \quad (38)$$

$$d = -\beta - \frac{bk_0^4}{R_0^2}, \tag{39}$$

$$e = 4\beta\left(1 - \frac{2k_0^4}{R_0^2}\right) + \frac{4k_0^2\zeta}{R_0^2}. \tag{40}$$

Since $a > 0$ Eq. (33) is well posed even when $\gamma < 0$.

Assuming that $v = O(\epsilon)$, $\partial_x = O(\epsilon)$, and $\partial_t = O(\epsilon^4)$ the terms in Eq. (33) are all of the same order provided we take γ and D are both $O(\epsilon^2)$. In this case the steepening from the Burgers term and the Benjamin-Feir instability all occur on the same time scale as its saturation via higher-order diffusion and nonlinearity. If this is the case the expansion becomes uniform in time and Eq. (33) formally describes the whole time evolution of any initial wave number distribution with only $O(\epsilon^{-1})$ spatial variation. This condition is valid for all b and β when

$$k_0^2 \sim \zeta = O(\epsilon^2). \tag{41}$$

B. The $K = O(1)$ case

The corresponding derivation for the case $K \neq 0$ is considerably more involved largely as a consequence of the slow drift identified in Eq. (12) when the modulation wave number k is small. As a result we write $\xi = x - ct$, where c is the (unknown) drift speed and write Eqs. (30) and (31) in the comoving frame:

$$\begin{aligned} R_t = {} & cR_\xi + rR - R^3 - k_0^4 R + \left[-2k_0^2 R_{\xi\xi} + 6K^2 R_{\xi\xi} + 12K R_\xi K_\xi - RK^4 + 2RK^2k_0^2 + 3RK_\xi^2 + 4KK_{\xi\xi}R - R_{\xi\xi\xi\xi}\right] \\ & + \beta\left[-4K^3 R_\xi + 6K_\xi R_{\xi\xi} + 4R_\xi K_{\xi\xi} + 4KR_\xi k_0^2 + 4KR_{\xi\xi\xi} - 6RK^2K_\xi + 2Rk_0^2K_\xi + RK_{\xi\xi\xi}\right] - \zeta[2R_\xi K + RK_\xi], \end{aligned} \tag{42}$$

$$\begin{aligned} K_t = {} & cK_\xi - 2bRR_\xi - \left[4\frac{R_{\xi\xi\xi}}{R}K + 6\frac{R_{\xi\xi}}{R}K_\xi + 4\frac{R_\xi}{R}K_{\xi\xi} + K_{\xi\xi\xi} - 4\frac{R_\xi}{R}K^3 - 6K^2K_\xi + 2k_0^2K_\xi + 4k_0^2K\frac{R_\xi}{R}\right]_\xi \\ & + \beta\left[-2k_0^2\frac{R_{\xi\xi}}{R} + 6K^2\frac{R_{\xi\xi}}{R} + 12KK_\xi\frac{R_\xi}{R} - K^4 + 2k_0^2K^2 + 3K_\xi^2 + 4KK_{\xi\xi} - \frac{R_{\xi\xi\xi\xi}}{R}\right]_\xi + \zeta\left[\frac{R_{\xi\xi}}{R} - K^2\right]_\xi. \end{aligned} \tag{43}$$

We next rewrite these equations in terms of amplitude and wave number perturbations u, v defined by $R = R_0(1+u)$, $K = K_0(1+v)$, where the subscript zero refers to the TW solution (9) with $R_0 = |u_0|$ and $K = K_0$. We solve the resulting equations on the assumption that both u and v are of order $\epsilon \ll 1$, and suppose that the ξ derivatives are of order ϵ as well; that is, we write $(u,v) \to \epsilon(\hat{u},\hat{v})$, $\xi \to \hat{\xi}/\epsilon$, where the quantities with a hat are formally of order one. In the calculation the drift at every order must be incorporated into the speed c. Thus, $c = c_0 + \epsilon c_1 + \epsilon^2 c_2 + \cdots$, and the remaining time derivative refers to growth arising from the real part of the unstable eigenvalue only; as shown below, this derivative enters the calculation at $O(\epsilon^3)$. Since v is the slow mode the perturbation u is slaved to the (slow) evolution of v and we write (omitting hats)

$$u = Av + \epsilon Bv^2 + \epsilon C v_\xi + \epsilon^2 Dv^3 + \epsilon^2 E v v_\xi + \epsilon^2 F v_{\xi\xi} + \cdots, \tag{44}$$

and assume that both u and v are functions of the slow times $\tau = \epsilon^2 t$ and $T = \epsilon^3 t$, that is, $u(\xi,t) = u(\xi,\tau,T)$, $v(\xi,t) = v(\xi,\tau,T)$. We summarize below the major steps in the derivation of the phase equation which we write in the form

$$\begin{aligned} K_0 v_t = {} & \epsilon^2 Q v_{\xi\xi} + \epsilon^2 S(v^2)_\xi + \epsilon^3 U v_{\xi\xi\xi} + \epsilon^3 V(vv_\xi)_\xi \\ & + \epsilon^3 W(v^3)_\xi + O(\epsilon^4), \end{aligned} \tag{45}$$

where $\partial_t = \epsilon^2\partial_\tau + \epsilon^3\partial_T$ and $Q,\ldots,W$ are coefficients depending on the parameters k_0, b, β, ζ, and the wave number K_0 of the basic wave train and computed below. Note that this equation is no longer equivariant with respect to $x \to -x$, $v \to -v$. This is a consequence of the nonzero value of the wave number K_0.

At $O(\epsilon)$ the above approach yields

$$A = \frac{2K_0^2(k_0^2 - K_0^2)}{R_0^2}, \tag{46}$$

while at $O(\epsilon^2)$ we find that

$$B = \frac{K_0^2}{R_0^2}(k_0^2 - 3K_0^2) - \frac{2K_0^4}{R_0^4}(k_0^2 - K_0^2)^2, \tag{47}$$

$$\begin{aligned} C = {} & \frac{K_0}{2R_0^2}\left\{-4\beta K_0^2 + \left[-\zeta + 2\beta(k_0^2 - K_0^2)\right]\right. \\ & \left.\times\left[\frac{4K_0^2(k_0^2 - K_0^2)}{R_0^2} + 1\right] + \frac{2c_0K_0}{R_0^2}(k_0^2 - K_0^2)\right\}, \end{aligned} \tag{48}$$

where c_0 is thus far unknown. Substituting these results into the v equation we obtain an equation of the form

$$K_0 v_t = \epsilon P v_\xi + \epsilon^2 c_1 v_\xi + \epsilon^2 Q v_{\xi\xi} + \epsilon^2 S(v^2)_\xi + O(\epsilon^3). \tag{49}$$

Since the drift is already incorporated in the drift speed c the $O(\epsilon)$ term on the right side cannot be balanced by the time derivative and we must therefore demand that $P = 0$, that is, that

$$c_0 = 4(b - \beta)K_0(k_0^2 - K_0^2) + 2\zeta K_0, \tag{50}$$

an expression that yields the result (12) for the frequency of small wave number perturbations. With this value of c_0 we see that v evolves on an $O(\epsilon^{-2})$ time scale in the comoving frame,

that is, on the time scale $\tau = O(1)$. Moreover, we also obtain expressions for the coefficients Q and S. Specifically,

$$\frac{Q}{K_0} = \zeta b - 2(1+\beta b)\left(k_0^2 - 3K_0^2\right) - \frac{8K_0^2}{R_0^2}(1+b^2)\left(k_0^2 - K_0^2\right)^2, \tag{51}$$

a result that agrees with the real part of the unstable phase mode eigenvalue given in Eq. (11), while

$$S = -K_0^2\left[\zeta + 2(b-\beta)\left(k_0^2 - 3K_0^2\right)\right]. \tag{52}$$

Finally, since the variable ξ is, by definition, the correct comoving frame, no additional drift may occur at $O(\epsilon^2)$ and we must take $c_1 = 0$. Thus, to $O(\epsilon)$ the evolution of the instability is described by Burger's equation [60],

$$K_0 v_\tau = Q v_{\xi\xi} + S(v^2)_\xi + O(\epsilon), \tag{53}$$

provided only that $Q/K_0 > 0$ so that diffusion arrests the steepening arising from the nonlinear term. We remark that $c_0 = -\partial\Omega/\partial K_0$ and $S = (1/2)K_0^2\partial^2\Omega/\partial K_0^2$, where $\Omega(K)$ is the dispersion relation (9b), in accord with general theory [61]. However, in the regime of greatest interest (the Benjamin-Feir unstable regime), the diffusion coefficient Q is destabilizing ($Q < 0$) and the Burger's problem is ill posed unless higher order terms are included. We calculate these terms next.

At $O(\epsilon^3)$ the equation for the evolution of the perturbation v includes the terms $c_2 v_\xi + U v_{\xi\xi\xi} + V(vv_\xi)_\xi + W(v^3)_\xi$, where

$$\begin{aligned} U &= -2bR_0^2F + 4K_0^3C - 4K_0k_0^2C \\ &\quad + \beta\left(-2k_0^2A + 6K_0^2A + 4K_0^2\right) + \zeta A \\ &= \left(4K_0^2/R_0^4\right)\left[-8b(1+b^2)K_0^2\left(k_0^2 - K_0^2\right)^3\right. \\ &\quad + (1+b^2)(k_0 - K_0)^2\left(\zeta - 2\beta k_0^2 + 6\beta K_0^2\right)R_0^2 \\ &\quad \left. - (b-\beta)R_0^4\right], \end{aligned} \tag{54}$$

$$\begin{aligned} V &= -2bR_0^2(AC+E) + 4K_0^3(2B - A^2 + 3A) \\ &\quad + 12K_0^3 - 4k_0^2K_0(A - A^2 + 2B) \\ &= \frac{4K_0^3}{R_0^4}\left[8(1+b^2)K_0^2\left(k_0^2 - K_0^2\right)^3 - 4(1+b^2)\left(k_0^4 - 4k_0^2K_0^2\right.\right. \\ &\quad \left.\left. + 3K_0^4\right)R_0^2 + 3(1+b\beta)R_0^4\right)\Big], \end{aligned} \tag{55}$$

and

$$W = -2bR_0^2(AB+D) - 4\beta K_0^4 = 4(b-\beta)K_0^4. \tag{56}$$

To evaluate the above expressions we computed the coefficients D, E, F in Eq. (44). Once again we may take $c_2 = 0$, obtaining

$$R_0^6 D = -2K_0^4\left[R_0^2 + \left(k_0^2 - K_0^2\right)^2\right]\left(R_0^2 - 2k_0^2K_0^2 + 2K_0^4\right), \tag{57}$$

$$\begin{aligned} R_0^6 E &= -24bK_0^5\left(k_0^2 - K_0^2\right)^3 - 6\beta K_0^3R_0^4 - R_0^2K_0^3\left(k_0^2 - K_0^2\right) \\ &\quad \times\left[\zeta - 2(2b+\beta)\left(k_0^2 - 3K_0^2\right)\right], \end{aligned} \tag{58}$$

$$\begin{aligned} R_0^6 F &= 2K_0^2\left[4(1+2b^2)K_0^2\left(k_0^2 - K_0^2\right)^3 - b\left(k_0^2 - K_0^2\right)\right. \\ &\quad \left.\times\left(\zeta - 2\beta k_0^2 + 6\beta K_0^2\right)R_0^2 + R_0^4\right]. \end{aligned} \tag{59}$$

The expressions for E and F include contributions from the leading order estimate of the term $u_\tau = Av_\tau + O(\epsilon)$. In view of Eq. (49) this term is $O(\epsilon^3)$ in unscaled variables.

Equation (45) generalizes Eq. (33) to the case $K_0 \neq 0$, that is, to long wave perturbations of TWs, and shows that even in the comoving frame the wave number perturbation v evolves on two time scales, $t = O(\epsilon^{-2})$ and $t = O(\epsilon^{-3})$. The perturbation grows and steepens on the faster time scale and only equilibrates on the slower time scale, once again indicating that if $Q < 0$ the resulting evolution is nonuniform in time.

When $Q < 0$, that is, $\mathrm{Re}\sigma_+ > 0$ [see Eq. (11) with $K = K_0$], the uniform wave number state ($v = 0$) is unstable. Near the threshold $Q = 0$ the time scale balance changes since the growth rate of the instability is slower than assumed in the above derivation. Specifically, if we take $Q = \epsilon^2\hat{Q}$, where $\hat{Q} = O(1)$, we must assume for consistency that $v = \epsilon w$. Here $w = O(1)$ and hence the unscaled wave number perturbation $v = O(\epsilon^2)$, that is, smaller than assumed in the derivation of Eq. (45) where the coefficients $Q, S, \ldots$ are all formally of order one. In this case w evolves on an $O(\epsilon^{-3})$ time scale and we write $w = w(\xi, T)$, where $T = \epsilon^3 t$. Repeating the above derivation we find that in the near-threshold regime $O(\epsilon^2)$ wave number perturbations obey the perturbed Korteweg-de Vries equation

$$\begin{aligned} &K_0 w_T - 2Sww_\xi - Uw_{\xi\xi\xi} \\ &\quad = \epsilon[\hat{Q}w_{\xi\xi} + V(ww_\xi)_\xi + Zw_{\xi\xi\xi\xi}] + O(\epsilon^2), \end{aligned} \tag{60}$$

derived in a number of previous studies [62–64]. Equation (60) is also known as the modified Kawahara equation [65,66] and in other regimes as the generalized Kuramoto-Sivashinsky equation [67]. Once again, in this equation the coefficients S, U, $\hat{Q}$, V, and Z are all formally of order one, with Z given by

$$\begin{aligned} Z &= -\frac{K_0^2}{2R_0^6}\left\{64(1+2b^2)K_0^4\left(k_0^2 - K_0^2\right)^4\right. \\ &\quad - 24bK_0^2\left(k_0^2 - K_0^2\right)^2\left(\zeta - 2\beta k_0^2 + 6\beta K_0^2\right)R_0^2 \\ &\quad + \left[\left(\zeta - 2\beta k_0^2\right)^2 + 4\left(8k_0^2 + 3\left(\zeta - 2\beta k_0^2\right)\beta\right)K_0^2\right. \\ &\quad \left.\left. - 4(8 - 9\beta^2)K_0^4\right]R_0^4 + 2R_0^6\right\}. \end{aligned} \tag{61}$$

In order that Eq. (60) be well posed we demand that $Z < 0$. When this is not the case a yet higher order calculation becomes necessary in order to identify terms that may arrest the resulting shortwave instability.

In writing Eq. (60) we have included $O(\epsilon)$ terms. These terms govern the evolution of w on yet longer time scale, $t = O(\epsilon^{-4})$, but are required in order to select among the different solutions of the leading order Korteweg-de Vries equation

$$K_0 w_T - 2Sww_\xi - Uw_{\xi\xi\xi} = 0. \tag{62}$$

The $O(\epsilon)$ terms are essential since the CSHE is a dissipative system while the Korteweg-de Vries equation (62) is conservative and completely integrable. As discussed below these higher order terms select the amplitude and speed (relative to the moving frame ξ) of both solitonlike solutions and cnoidal solutions which is undetermined within (62),

a process that takes place on an $O(\epsilon^{-4})$ time scale as discussed in Refs. [63,65,68,69]. Following [63] we obtain the solution

$$w = N\mathrm{sech}^2[\rho(\xi - sT)] + O(\epsilon), \tag{63}$$

where

$$\rho = \sqrt{SN/6U}, \quad s = -2SN/3K_0. \tag{64}$$

The amplitude of this solution evolves on the slower time scale $T' \equiv \epsilon T$ according to the (corrected) equation

$$\frac{dN}{dT'} = -\frac{8}{945}\frac{SN^2}{K_0U^2}[21\hat{Q}U - (10SZ - 12UV)N]. \tag{65}$$

Consequently, we expect, in this regime, the presence of solitons of amplitude

$$N_0 = \frac{21\hat{Q}U}{10SZ - 12UV}. \tag{66}$$

Within the perturbed Korteweg-de Vries equation these solitary waves are amplitude-stable whenever $K_0S(12UV - 10SZ) > 0$. An example of such a solitary wave solution is shown in Fig. 13(a) for parameter values such that the coefficients in the perturbed Korteweg-de Vries equation (60) are all O(1), with $Q < 0$, $Z < 0$ and ϵ small, while Fig. 13(b) shows the soliton in panel (a), appropriately rescaled, in terms of the corresponding wave number perturbation in the CSHE. Such a choice demands a fine-tuning of the CSHE parameters as the coefficients $S, Q \ldots$ can be very sensitive to changes in these parameters. Since the length scale in the system has been defined by demanding that $|\hat{Q}| = |K_0|$, implying that $\epsilon = \sqrt{|Q|/|K_0|}$, we can only regard Eq. (60) as a perturbation of the Korteweg-de Vries equation (62) if the coefficient Q is small. Figures 14(a) and 14(b) show the dependence of Q on ζ and K_0, with the remaining parameters as in Fig. 13(a). Thus, Q is negative and small only when (a) $\zeta \approx -0.1$ ($K_0 = 0.505$) and (b) $K_0 \approx 0.5$ ($\zeta = -0.1$), motivating the choice of parameters used in Fig. 13(a). Panels (c) and (d) of Fig. 14 show the corresponding variation in ρ, while panels (e) and (f) depict the variation in the amplitude N_0 of the soliton solution. For this parameter set, only dark solitons ($N_0 < 0$) exist close to $Q \approx 0$, representing a localized dilation of the wavelength of the original wave train. We mention that numerical simulations of TW doubly diffusive convection reveal steadily traveling compression pulses ($N_0 > 0$) in appropriate parameter regimes [70]. We study solitary wave solutions in the perturbed Korteweg-de Vries equation (60) and in the CSHE in Sec. VI B.

Because of the absence of oscillatory tails the Korteweg-de Vries solitons do not form bound states. However, bound states form for larger values of ϵ when additional terms enter into the equation, and the solitary wave becomes asymmetric. This is so both for the modified Kawahara equation [64] and for the convective Cahn-Hilliard equation [71], suggesting that the observation of traveling bound states in the CSHE such as those in Figs. 10(a) and 10(b) is likely a common occurrence. Similar bound states form in the generalized Kuramoto-Sivashinsky equation, that is, Eq. (60), with $\epsilon = O(1)$ and $V = 0$ [67].

The Korteweg-de Vries equation (62) also admits spatially periodic, traveling solutions called cnoidal waves. These take the form

$$w_{cn} = w_0 + N\mathrm{cn}^2\left(\frac{1}{k_{cn}}\sqrt{\frac{SN}{6U}}\left[\xi - \frac{2S\left(-3k_{cn}^2w_0 + N - 2k_{cn}^2N\right)}{3K_0k_{cn}^2}T\right], k_{cn}\right), \tag{67}$$

parametrized by w_0, k_{cn}, and the amplitude N. The elliptic modulus k_{cn} is determined by the spatial period L of the domain. If the domain contains n wavelengths,

$$L = n\Gamma(k_{cn}) = 2nK(k_{cn})k_{cn}\sqrt{\frac{6U}{SN}} = 2nk_{cn}\sqrt{\frac{6U}{SN}}\int_0^{\pi/2}\frac{1}{\sqrt{1 - k_{cn}^2\sin^2 s}}ds. \tag{68}$$

In order that w_{cn} represent a perturbation of the basic wave number K_0 it must satisfy the condition $\int_0^L w_{cn}(\xi)d\xi = 0$. This requirement determines the quantity w_0. Finally, the amplitude N of the cnoidal solution is selected by the perturbation terms on the right side of Eq. (60). To determine N we multiply both

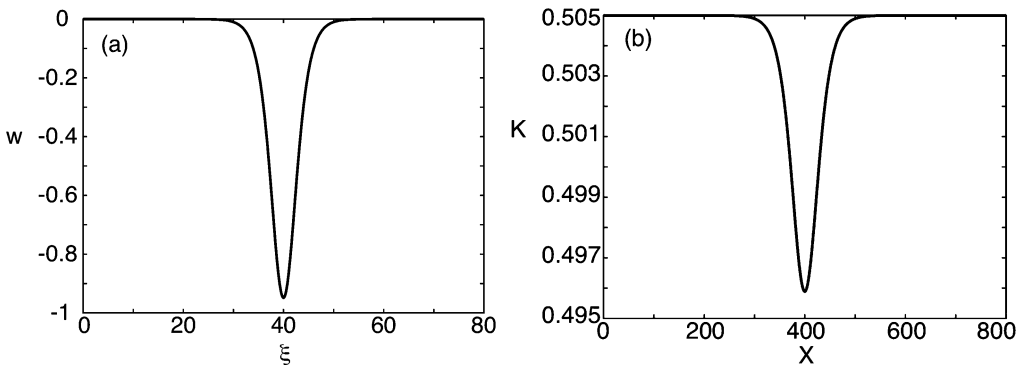

FIG. 13. (a) A soliton solution in the perturbed Korteweg-de Vries equation (60) for $b = -1$, $\beta = 0.9$, $\zeta = -0.1$, $K_0 = 0.505$, $k_0 = 0.1$, and $r = 1$, corresponding to the coefficient values $S = -0.7062$, $U = 1.199$, $\hat{Q} = -K_0 = -0.505$, $V = -0.6916$, $Z = -0.5397$, $\epsilon = 0.098$. (b) The solution (a) interpreted within the CSHE as a perturbation of the wave number K (here a localized wavelength dilation).

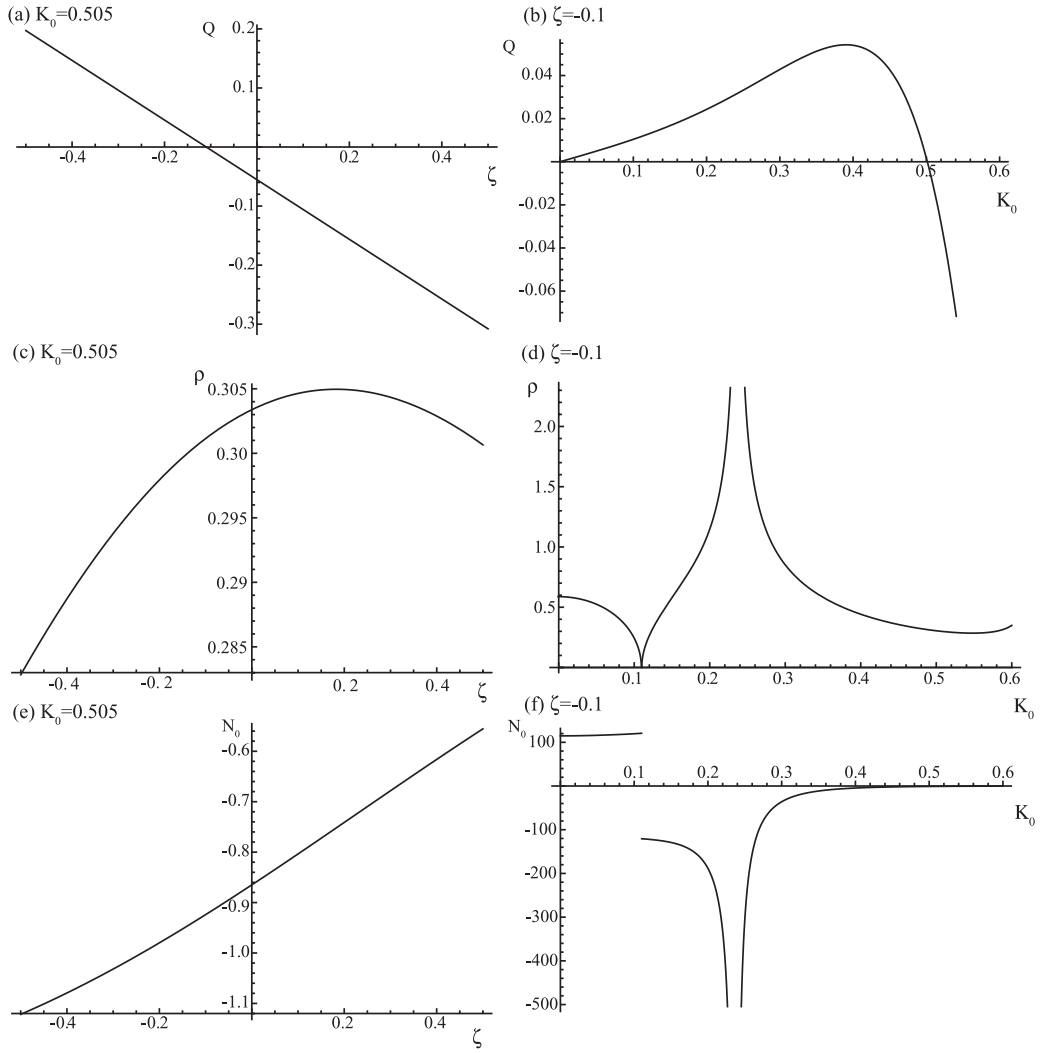

FIG. 14. The quantities Q, ρ, and N_0 characterizing soliton solutions of the perturbed Korteweg-de Vries equation (60) as functions of ζ and K_0, with $b = -1$, $\beta = 0.9$, $k_0 = 0.1$, and $r = 1$ kept fixed.

sides of Eq. (60) by $w(\xi - cT)$, where $c = 2S(-3k_{cn}^2 w_0 + N - 2k_{cn}^2 N)/3K_0 k_{cn}^2$, and integrate over the period L/n. The left side of the resulting equation vanishes after integration by parts. Since $w = w_{cn} + O(\epsilon)$ the terms on the right side may be evaluated using the approximation $w = w_{cn}$, resulting in an implicit expression for N. Solving this relation for the parameter values of Fig. 13 gives $N = -1.729\,15$. The corresponding value of w_0 is 0.644 367. This solution is shown in Fig. 15(a) and its interpretation as a perturbation of the wave number K_0 is given in Fig. 15(b). In Sec. VI B we compare these solutions with numerical simulations of the perturbed Korteweg-de Vries equation and the CSHE and demonstrate that these solutions are indeed realized in the numerical simulations and persist over long times.

VI. DYNAMICS OF THE NONLINEAR PHASE EQUATIONS

In this section we numerically explore the dynamical behavior of the nonlinear phase equations (33) and (60) derived in the previous section and compare the results with the dynamics observed in the CSHE.

A. The generalized convective Cahn-Hilliard equation ($|K| \ll 1$)

An important limit of Eq. (33) describing perturbations of the homogeneously oscillating state $K_0 = 0$ is obtained on the assumption that k_0 is small, $k_0 = O(\epsilon)$ (in Sec. IV $k_0 = 0.2$), while assuming that $\zeta = 0$. In this regime, Eq. (33) simplifies to

$$v_t = \left[-2k_0^2(1+b\beta)v - v_{xx} + 2v^3\right]_{xx} + \left[2k_0^2(\beta - b)v^2 + \beta\left(3v_x^2 - v^4 + 4vv_{xx}\right)\right]_x. \quad (69)$$

In this equation all terms are formally $O(\epsilon^5)$, and we define ϵ by setting $k_0 = \epsilon$. The resulting equation may be rescaled, leading to

$$v_{T'} = \left[-2(1+b\beta)v - v_{xx} + 2v^3\right]_{xx} + \left[2(\beta - b)v^2 + \beta\left(3v_x^2 - v^4 + 4vv_{xx}\right)\right]_x. \quad (70)$$

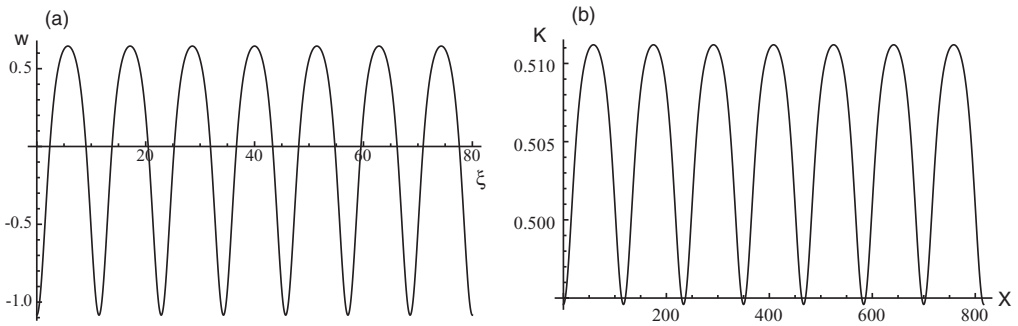

FIG. 15. (a) A cnoidal wave solution consisting of seven wavelengths in the perturbed Korteweg-de Vries equation (60) for $b = -1$, $\beta = 0.9$, $\zeta = -0.1$, $K_0 = 0.505$, $k_0 = 0.1$, $r = 1$, and $L = 80$, corresponding to the coefficient values $S = -0.7062$, $U = 1.199$, $\hat{Q} = -K_0 = -0.505$, $V = -0.6916$, $Z = -0.5397$, $\epsilon = 0.098$. (b) The solution (a) interpreted within the CSHE as a perturbation of the wave number K_0.

1. $b \neq 0, \beta = \zeta = 0$

Equation (70) helps us to understand the dynamical behavior of the CSHE observed in Sec. IV A 1 for $k_0 = 0.2$, $r = 1$, and $\beta = \zeta = 0$. In this regime, Eq. (70) becomes the convective Cahn-Hilliard equation,

$$v_{T'} = [-2v - v_{xx} + 2v^3]_{xx} - 2b[v^2]_x. \tag{71}$$

As in Sec. IV A 1, we explore the dynamics described by the convective Cahn-Hilliard equation (71) using direct numerical simulation, starting with small values of b for which coarsening is observed in the CSHE. We use small amplitude noise as initial condition and choose $L = 60$ as the domain length, equivalent to the larger domain length $L = 300$ in our simulations of the CSHE if one takes into account the scaling $X = k_0 x$ in the phase equation (70).

Figure 16(a) (top panel), demonstrates that for small values of b coarsening behavior is indeed observed. Due to the initial instability the system first develops a periodic solution (about nine peaks in the chosen domain $L = 60$), which then coarsens in time until only one domain remains. The lower panel shows the final state ($T = 2000$). This coarsening behavior for small values of b is consistent with the behavior observed in the CSHE (see, e.g., Fig. 3); similar behavior has been seen in earlier studies of the convective Cahn-Hilliard equation [59,71,72]. Note that the time scales in Figs. 3 and 16(a) differ by several orders of magnitude owing to the difference in the scaling of the time coordinate ($T = k_0^4 t$). When b is more negative [Figs. 16(b) and 16(c)] the system still coarsens after the initial instability, but this coarsening is arrested before only one domain remains. Instead, the long time solution is periodic with N maxima, $N = 2$ in Fig. 16(b) and $N = 4$ in Fig. 16(c). Although such periodic states are the long time attractor when the system is initialized with small amplitude noise, we have verified that in this regime these arrested states coexist with a stable $N = 1$ state, similar to the one domain solution in panel (a), in agreement with the CSHE results. Figures 16(d) and 16(e) show two different realizations when $b = -2$, both starting from small amplitude noise. In each case the system goes through an irregular initial transient during which several peaks undergo fast localized oscillations and may merge with each other, but the long time stable solution consists of a TW consisting of a train of pulses all moving with the same speed, some with superposed rapid oscillations [see, e.g., panel (d)], as also reported in Ref. [59]. We remark that similar solutions are observed in the CSHE [see, e.g., Fig. 4(b)]. A further decrease of b extends the initial period of fast oscillations and results in long time chaotic behavior, as shown in Fig. 16(f).

When $b \to 0$, Eq. (71) reduces to the Cahn-Hilliard equation, originally derived to describe the dynamics of phase separation in systems with a conserved quantity in the context of binary alloys [41]. The coarsening dynamics identified in our numerical simulations in Sec. IV A 1 for small values of b (see Fig. 3) are consistent with the Cahn-Hilliard description of the dynamics in this regime. As $|b|$ increases the Cahn-Hilliard description breaks down and the dynamics are described by Eq. (71) in which nonlinear advection plays an increasing role. It is this term that is ultimately responsible for the presence of chaotic dynamics in this system. Indeed, in the limit $b \to \infty$, Eq. (71) reduces to the Kuramoto-Sivashinsky equation [26,31]. Figure 6 confirms the presence of a transition toward spatiotemporal chaos as $|b|$ increases.

2. $b \neq 0, \beta \neq 0, \zeta = 0$

When β is no longer zero (see Sec. IV A 2), the situation becomes more complicated since Eq. (69) no longer reduces to either the Cahn-Hilliard or Kuramoto-Sivashinsky equations. However, the convective Cahn-Hilliard part of the equation continues to dominate the numerically observed behavior. In Fig. 17 we show the β dependence of the instability growth rate γ and of the coefficient D of the advective term for $b = -1$, $\zeta = 0$. The coefficient γ passes through zero at $\beta = 1$; the homogeneous steady state is unstable for $\gamma < 0$ ($\beta < 1$). In contrast, TWs with wave number $K = k_0$ are stable for $\gamma < 0$ and unstable for $\gamma > 0$ [see Eq. (13)]. As already mentioned the change of sign of γ corresponds to the well-known Benjamin-Feir (BF) instability of TWs. The BF instability therefore occurs whenever $1 + b\beta < 0$, much as for the CGLE. In the figure we show, in addition, the locations where magnitudes of γ and $D/2$ are equal. This condition is given by $1 + b + (b - 1)\beta = 0$ (for $\gamma = -D/2$) or $1 - b + (b + 1)\beta = 0$ (for $\gamma = D/2$) and this line provides an order of magnitude estimate of the location of the transition from Cahn-Hilliard-type dynamics to Kuramoto-Sivashinsky-type dynamics.

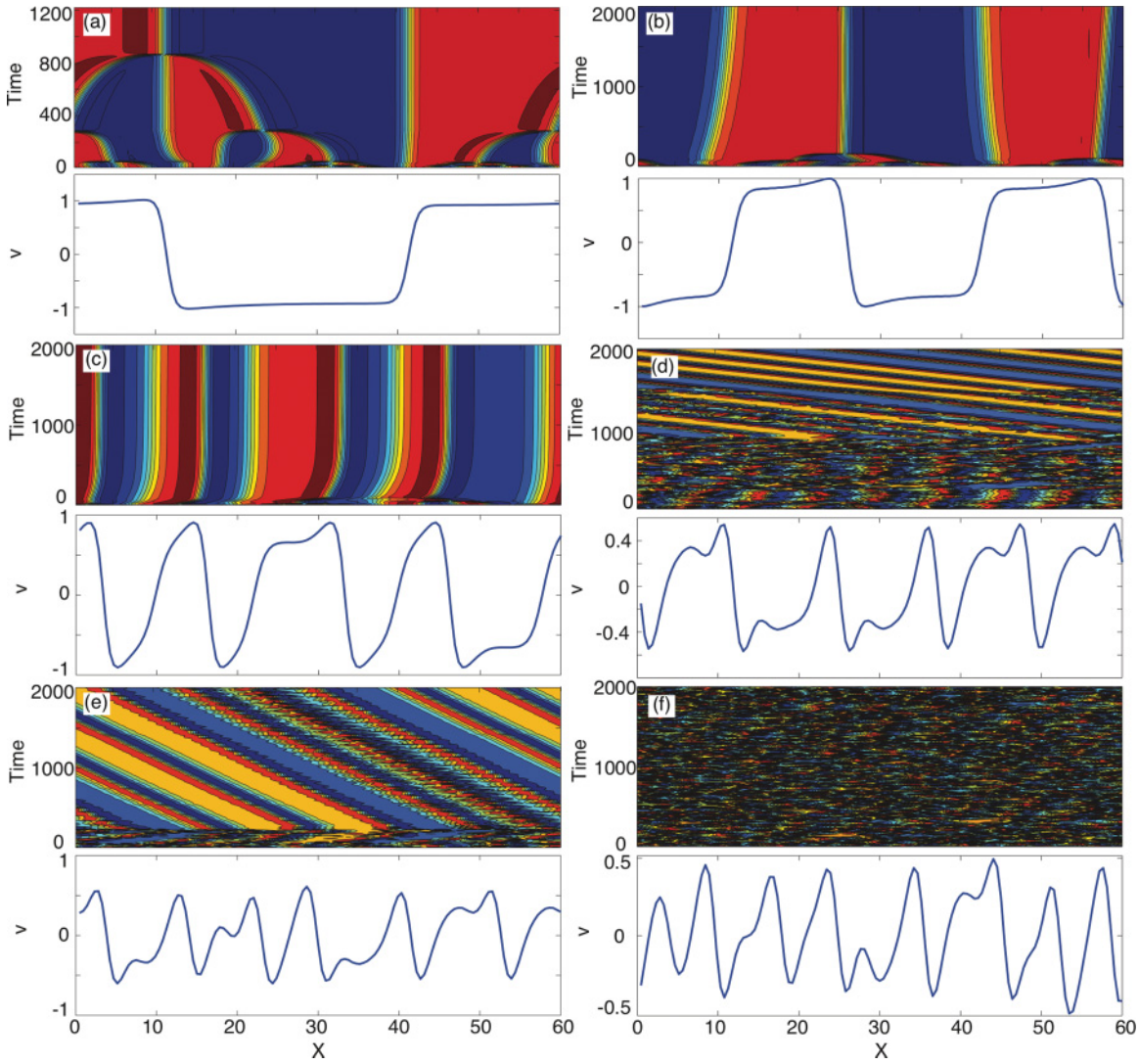

FIG. 16. (Color online) Temporal simulation of the nonlinear phase equation (70) in terms of space-time plots of the time evolution of the local wave number v. Red (light gray)/blue (dark gray) correspond to high/low values of v. Parameters: $L = 60$, $N = 128$, $\beta = 0$, $b = -0.15$, (a) -0.3, (b) -0.6, (c) -2 (d) and (e), and -3 (f).

Let us now focus on $b = -1$, the value used in the numerical simulations of Sec. IV A 2. For negative values of β (region I in Fig. 17), one can see that $\gamma < 0$ and $|\gamma| > |D/2|$. In this region homogeneous oscillations are unstable with leading order dynamics given by the convective Cahn-Hilliard equation with a small advective term whose magnitude is specified by the value of D. Thus, coarsening is expected, in agreement with Fig. 7.

When $0 < \beta < 1$ (region II in Fig. 17), homogeneous oscillations are still unstable ($\gamma < 0$), but the magnitude of the advective term $D/2$ now exceeds that of γ. Thus, in region II Eq. (69) resembles the Kuramoto-Sivashinsky equation rather than the Cahn-Hilliard equation, and indeed in this region coarsening dynamics are no longer observed.

In Fig. 18(a) we choose b and β such that $1 + b\beta = 0.2$ in order to be close to the BF instability and hence in the regime of validity of the phase equation (70). The figure shows that for nonzero β the different maxima undergo random zigzag motion. Similar back-and-forth motion of LSs is observed in Figs. 18(b) and 18(c), in agreement with the type of spatiotemporal intermittency observed in the CSHE at these parameter values [Figs. 6(c)–6(f)]. Indeed, in this regime one observes apparently random switching between two types of dynamics, laminar dynamics in which the solution resembles stable TWs, and turbulent dynamics consisting of strongly interacting LSs [31]. The numerically determined transition points to this state are plotted in the (b,β) plane in Fig. 17(b) using gray dots and confirm that the location of the transition is very well approximated by the condition $|\gamma| \approx |D/2|$.

In region III ($\beta > 1$), the TWs are unstable but the homogeneous oscillation is stable ($\gamma > 0$). Here the convective term $D/2$ is larger in magnitude than γ and Eq. (70) looks more and more like a Kuramoto-Sivashinsky-type equation. For β slightly larger than 1, stable periodic variation of the wave number K is found (not shown). Increasing β further these periodic solutions develop additional spatial modulation (cf. Fig. 9); this modulation becomes more pronounced and irregular with increasing β. We remark that in the transition

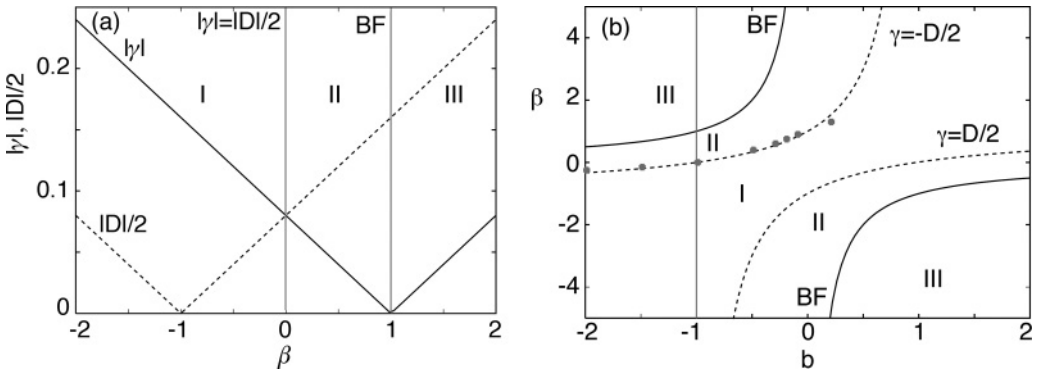

FIG. 17. (a) The coefficients $\gamma \equiv -2k_0^2(1+b\beta)$ and $D/2 \equiv 2k_0^2(\beta - b)$ in Eq. (69) as functions of the parameter β for $k_0 = 0.2$ and $b = -1$. (b) Transition from coarsening behavior to spatiotemporal intermittency in the (b,β) plane (gray dots), together with the locus of the Benjamin-Feir (BF) instability Eq. (7) and the locus of the points where γ and $D/2$ are equal in magnitude. The transition from coarsening behavior to spatiotemporal intermittency has been determined numerically with an accuracy $\Delta\beta = 0.1$.

from region II (spatiotemporal intermittency) to region III where periodic solutions exist, *freezing* occurs [31], stabilizing states with a spatially disordered structure. Such a stably drifting disordered solution can be seen in Fig. 8 ($\beta = 1$).

B. The perturbed Korteweg-de Vries equation [$K = O(1)$]

In Sec. V B, we showed that for $O(\epsilon^2)$ perturbations of the local wave number of a TW in the CSHE, the wave number perturbation evolves according to the perturbed Korteweg–de Vries equation [see Eq. (60)]. The predicted solitary wave solutions of this equation are found in the CSHE in appropriate parameter regimes. We choose the values $b = -1$, $\beta = 0.9, \zeta = -0.1, K_0 = 0.505, k_0 = 0.1$, and $r = 1$. Solving the CSHE with these parameter values reveals structures resembling Fig. 13(b) except for a shift in the background owing to finite domain length (cf. Ref. [70]). Thus, the corresponding solution of the CSHE is given by the expression

$$K(x,t) = K_0 + \epsilon^2 N_0 \mathrm{sech}^2[\epsilon\rho(x - v_{sw}t)], \tag{72}$$

where $N_0 = -0.949$ (implying localized dilation), $\epsilon = 0.098$, and $\rho = 0.296$. The drift speed of the solitary wave is $v_{sw} = c_0 + \epsilon^2 s$ [Eq. (64b)], where $s = -0.884$, and is dominated by the TW speed for $K_0 \neq 0$, viz., $c_0 = 0.839$.

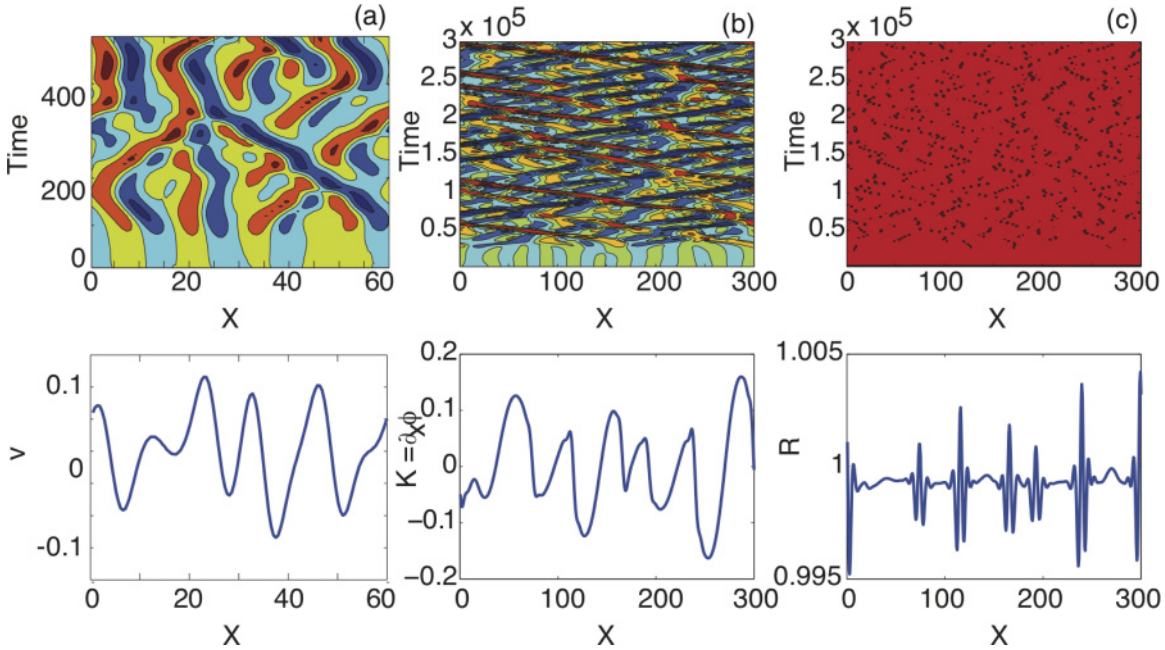

FIG. 18. (Color online) (a) Temporal simulation of the nonlinear phase equation (70). The top panel shows a space-time plot of the time evolution of the local wave number v. Red (light gray)/blue (dark gray) correspond to high/low values of v. The bottom panel shows the profile of v at the final time step $T = 500$. Parameters: $L = 60$, $N = 128$, $b = -1$, $\beta = 0.8$. Panels (b) and (c) show, for the same parameter values, the space-time evolution of the wave number K and the amplitude R for the CSHE (1). The bottom panels show the profiles at the final time $t = 3 \times 10^5$. Parameters: $L = 300$, $N = 1024$, $b = -1$, $\beta = 0.8$, $k_0 = 0.2$.

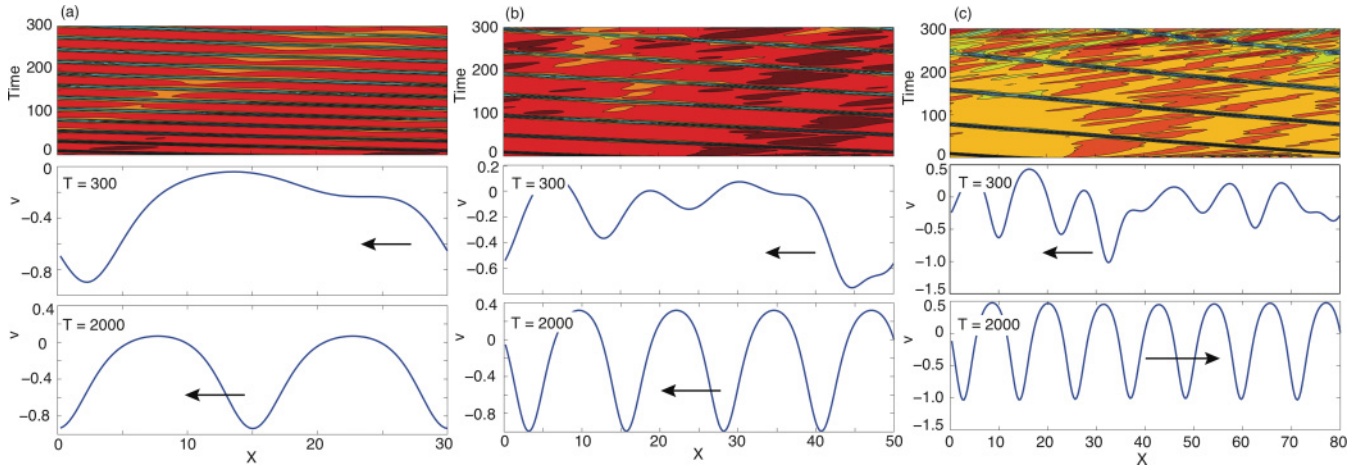

FIG. 19. (Color online) Temporal simulation of the perturbed Korteweg-de Vries equation (60) in terms of space-time plots showing the time evolution of the local wave number w. Red (light gray)/yellow-blue (dark gray) correspond to high/low values of w. The middle and bottom panels show the intermediate solution at $T = 300$ and the final solution at $T = 2000$, respectively. Parameters: $S = -0.7062$, $U = 1.199$, $\hat{Q} = -K_0 = -0.505$, $V = -0.6916$, $Z = -0.5397$, $\epsilon = 0.098$, and $N = 256$. (a) $L = 30$, (b) $L = 50$, (c) $L = 80$. The final state in case (c) resembles closely the analytical prediction depicted in Fig. 15(a).

We now examine the dynamical behavior of the above solitary wave in the perturbed Korteweg-de Vries equation (60). Using $w = 1.5N_0\text{sech}^2\rho\xi$ as an initial condition we evolve Eq. (60) in time for 300 and 2000 time units and repeat this for three different domain widths, $L = 30,50,80$. The results are shown in Fig. 19. For small domain widths [see Fig. 19(a), $L = 30$], the initial sech^2 profile with amplitude $1.5N_0$ quickly relaxes to its preferred amplitude N_0 and this solution then travels with a constant speed $s \approx -0.884$, as predicted. For small L this solitary wave may remain stable in time. However, for larger domain lengths the background state becomes unstable with respect to longwave perturbations since the background wave number is BF unstable ($\hat{Q} < 0$, $Z < 0$). The growth of this instability eventually disrupts the solitary wave, a process that occurs increasingly rapidly as L increases [see Figs. 19(b) and 19(c)]. However, the final state closely resembles the cnoidal solution depicted in Fig. 15(b) and computed analytically from the perturbed Korteweg-de Vries equation [Fig. 19(c)]. The correspondence between the analytical solution and the simulation results becomes increasingly good as the initial perturbation around $w = 0$ decreases.

Let us now turn to the CSHE. As initial condition we take a spatial oscillation with wave number K and amplitude $\sqrt{r - k_0^4}$ with the wave number perturbation shown in Fig. 19(b) superposed, scaled as in Eq. (72). We scale the domain length $L \to L/\epsilon$ and take particular care in matching the phase at the boundaries to satisfy the periodic boundary conditions in the CSHE. Since the evolution in the CSHE occurs on an $O(\epsilon^{-3})$ time scale relative to the evolution time scale for the perturbed Korteweg-de Vries equation (60) we evolve the CSHE for $300/(\epsilon^3) \approx 3 \times 10^5$ and $2000/(\epsilon^3) \approx 2 \times 10^6$ time units. Figure 20 shows the results of these simulations for three different domain lengths, $L \approx 300,500,800$. The figure shows the phase gradient profile after evolving the system for $t = 3 \times 10^5$ (top panels) and $t = 2 \times 10^6$ (bottom panels).

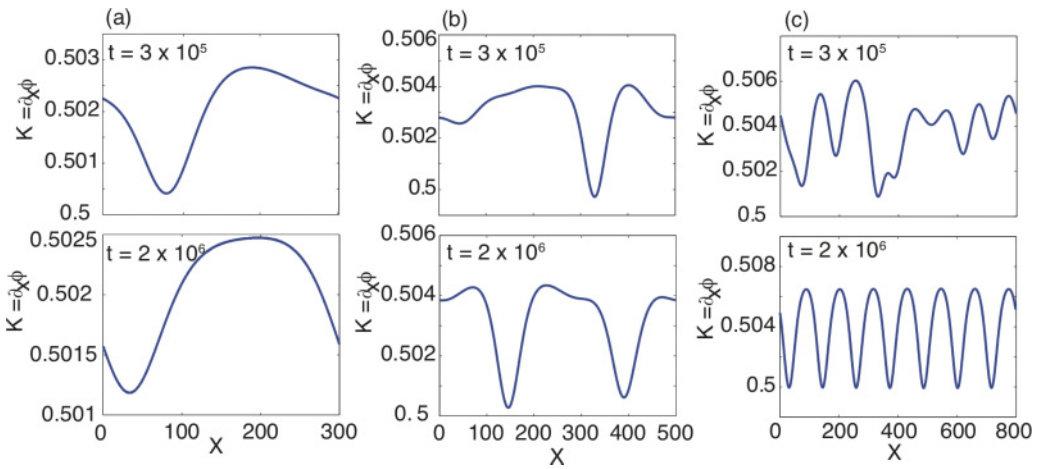

FIG. 20. (Color online) Temporal simulation of the CSHE for different values of the domain length L showing the profile of the local wave number K after $t = 3 \times 10^5$ (top panels) and $t = 2 \times 10^6$ (bottom panels). Parameters: $b = -1$, $\beta = 0.9$, $\zeta = -0.1$, $K_0 = 0.505$, $k_0 = 0.1$, $r = 1$, and $N = 1024$. $L \approx 300$, (a) 500, (b) and 800 (c).

The profile of K evolves on the slow time scale $T = \epsilon^3 t$, while the whole structure travels with approximate speed v_{sw} on the much faster time scale t, resulting in a large separation of time scales. Moreover, since finite size effects reduce the growth rate of the longwave instability, at any given time a simulation in a larger domain will be closer to its final state than one in a shorter domain. Thus, the solutions in panels (a) and (b) are still evolving toward the final cnoidal state even at $t = 2 \times 10^6$ while the solution (c) appears to have already reached this state. The result shown in Fig. 20(c) corresponds very well with the behavior observed in the perturbed Korteweg-de Vries equation in terms of both the structure wavelength and its amplitude [Fig. 19(c)]. Here, too, the uniform background state destabilizes when the domain length L increases and does so faster for larger values of L, eventually destroying the initial solitary wave and forming a spatially periodic traveling structure that closely resembles the cnoidal solution of the perturbed Korteweg-de Vries equation [Fig. 19(c)]. Similar states consisting of a periodic array of deep troughs have been observed in numerical simulations of a thin liquid film flowing down a heated inclined plane [73]. This type of behavior remains valid for $O(1)$ values of ϵ, for which the evolution and translation times becomes comparable not only to one another, but also to the steepening time scale for the Burger's equation (53).

VII. CONCLUSION

In this work, we have numerically explored the dynamical behavior that can arise in the CSHE with complex coefficients. With complex coefficients the equation is no longer variational and persistent time-dependence becomes possible. This time-dependence may take the form of drifting structures that are steady in the comoving frame or stationary oscillations superposed on top of a steady state. In the former case one typically finds defects in the form of sources and sinks of TWs which may drift and either annihilate, leading to gradual coarsening of the structure, or form bound states that drift together with a common speed. In other cases one finds that fronts separating two distinct states may undergo oscillatory instability, leading to persistent breathing, which can be periodic in time or chaotic. Many of our solutions resemble the states found in CCGLEs [26]. In the latter system these states arise from the competition between left- and right-traveling waves, while in our system such states are intrinsic. This is, of course, a consequence of the fact that the Swift-Hohenberg equation is reversible in space and that it selects a finite wave number at onset. This wave number, depending on its sign, generates left- or right-traveling waves which can then interact as in the CCGLEs. Indeed, we have seen that near onset the CSHE does reduce to the CCGLEs. In contrast, a single CGLE, though superficially resembling the CSHE, selects at onset wave number $k = 0$ and hence homogeneous oscillations. Thus, no traveling waves are present near onset; if a group velocity term is present waves are generated but these all travel in a preferred direction selected by the group velocity term. Thus, counterpropagating waves are absent.

Our computations revealed a variety of regimes with complex spatiotemporal dynamics, including the remarkable transition shown in Fig. 11 that resembles quantum mechanical tunneling. In all cases we have employed periodic boundary conditions. With these boundary conditions spatiotemporal chaos is likely a persistent feature of the equation. However, a recent study of the CGLE showed that with Neumann boundary conditions the complex dynamics eventually decay, although the characteristic decay times are exponential in the domain length L [74]. Whether this is also the case for the CSHE remains a question of some interest.

In order to shed light on the origin of the complex behavior we have, in addition, derived phase equations describing the slow evolution of the gradient of the spatial phase, that is, of the local wave number. This equation is of fourth order in space, and so is in principle simpler than the eighth order CSHE. We considered two cases. In the first we considered large scale spatial modulation of homogeneous oscillations in time and derived an equation generalizing the convective Cahn-Hilliard equation [see Eq. (33)]. In the second we considered slow modulation of a TW and derived two distinct types of equations depending on the amplitude of the modulation. For $O(\epsilon^2)$ amplitudes the local wave number evolves according to the generalized Kawahara equation, that is, a perturbed Korteweg-de Vries equation [see Eq. (60)], while for $O(\epsilon)$ amplitudes the local wave number obeys Burger's equation at leading order [60], perturbed by three higher order terms [see Eq. (45)]. The convective Cahn-Hilliard equation (71) describes a coarsening process when $|b|k_0 < 1/6$ [71], but for $|b|k_0 > 1/6$ we expect gradual freezing of the structures owing to the presence of oscillatory tails. Similar fronts are also found in the perturbed Burger's equation describing the evolution of Benjamin-Feir unstable modes, although smaller amplitude localized compressions of a TW state are found to obey a perturbed Korteweg-de Vries equation. We have shown that in appropriate parameter regimes, close to the Benjamin-Feir boundary, the phase equations do indeed capture much of the behavior of the CSHE. However, further away from this boundary the amplitude and phase dynamics become dynamically independent, greatly enlarging the range of possible behavior.

ACKNOWLEDGMENTS

We acknowledge helpful discussions with J. Mason. This work was supported in part by the National Science Foundation under Grant No. DMS-0908102. L.G. acknowledges support by the Research Foundation-Flanders (FWO-Vlaanderen).

[1] M. Cross and P. Hohenberg, Rev. Mod. Phys. **65**, 851 (1993).
[2] F. T. Arecchi, S. Boccaletti, and P. Ramazza, Phys. Rep. **318**, 1 (1999).
[3] R. Hoyle, *Pattern Formation: An Introduction to Methods* (Cambridge University Press, Cambridge, 2006).
[4] A. C. Newell and J. Whitehead, J. Fluid Mech. **38**, 279 (1969).

[5] I. S. Aranson and L. Kramer, Rev. Mod. Phys. **74**, 99 (2002).
[6] B. A. Malomed, Z. Phys. B **55**, 241 (1984).
[7] M. Bestehorn and H. Haken, Phys. Rev. A **42**, 7195 (1990).
[8] J. Swift and P. C. Hohenberg, Phys. Rev. A **15**, 319 (1977).
[9] P. Manneville, Theor. Comput. Fluid Dyn. **18**, 169 (2004).
[10] S. M. Cox, P. C. Matthews, and S. L. Pollicott, Phys. Rev. E **69**, 066314 (2004).
[11] A. Buka, B. Dressel, L. Kramer, and W. Pesch, Chaos **14**, 193 (2004).
[12] A. Golovin, B. Matkowsky, and A. Nepomnyashchy, Physica D **179**, 183 (2003).
[13] S. Longhi and A. Geraci, Phys. Rev. A **54**, 4581 (1996).
[14] V. J. Sánchez-Morcillo, E. Roldán, G. J. de Valcárcel, and K. Staliunas, Phys. Rev. A **56**, 3237 (1997).
[15] K. Staliunas, G. Slekys, and C. O. Weiss, Phys. Rev. Lett. **79**, 2658 (1997).
[16] K. Staliunas, M. F. H. Tarroja, G. Slekys, C. O. Weiss, and L. Dambly, Phys. Rev. A **51**, 4140 (1995).
[17] J. Lega, J. V. Moloney, and A. C. Newell, Phys. Rev. Lett. **73**, 2978 (1994).
[18] J. Lega, J. V. Moloney, and A. C. Newell, Physica D **83**, 478 (1995).
[19] J.-F. Mercier and J. V. Moloney, Phys. Rev. E **66**, 036221 (2002).
[20] J. M. Soto-Crespo and N. Akhmediev, Phys. Rev. E **66**, 066610 (2002).
[21] G. L. Oppo, A. J. Scroggie, and W. J. Firth, Phys. Rev. E **63**, 066209 (2001).
[22] M. Santagiustina, E. Hernandez-Garcia, M. San-Miguel, A. J. Scroggie, and G. L. Oppo, Phys. Rev. E **65**, 036610 (2002).
[23] P. Coullet, L. Gil, and F. Rocca, Opt. Commun. **73**, 403 (1989).
[24] A. C. Newell and J. V. Moloney, *Nonlinear Optics* (Addison-Wesley, Redwood City, CA, 1992).
[25] P. K. Jakobsen, J. V. Moloney, A. C. Newell, and R. Indik, Phys. Rev. A **45**, 8129 (1992).
[26] M. van Hecke, C. Storm, and W. van Saarloos, Physica D **134**, 1 (1999).
[27] J. Pedrosa, M. Hoyuelos, and C. Martel, Eur. Phys. J. B **66**, 525 (2008).
[28] F. Prati and L. Columbo, Phys. Rev. A **75**, 053811 (2007).
[29] G.-L. Oppo, A. M. Yao, F. Prati, and G. J. de Valcárcel, Phys. Rev. A **79**, 033824 (2009).
[30] L. Gelens and E. Knobloch, Eur. Phys. J. D **59**, 23 (2010).
[31] H. Chaté, Nonlinearity **7**, 185 (1994).
[32] J. Lega, Physica D **152–153**, 269 (2001).
[33] W. van Saarloos, Phys. Rep. **386**, 29 (2003).
[34] P. Coullet, T. Frisch, and F. Plaza, Physica D **62**, 75 (1993).
[35] B. A. Malomed, A. A. Nepomnyashchy, and M. I. Tribelsky, Phys. Rev. A **42**, 7244 (1990).
[36] H. Sakaguchi and B. Malomed, Physica D **118**, 250 (1998).
[37] B. Sandstede and A. Scheel, SIAM J. Appl. Dyn. Syst. **3**, 1 (2004).
[38] G.-K. Harkness, W. J. Firth, J. B. Geddes, J. V. Moloney, and E. M. Wright, Phys. Rev. A **50**, 4310 (1994).
[39] H. Leblond, M. Brunel, D. Amroun, and F. Sanchez, J. Opt. A: Pure Appl. Opt. **7**, 56 (2005).
[40] P. V. Paulau, A. J. Scroggie, A. Naumenko, T. Ackemann, N. Loiko, and W. J. Firth, J. Opt. A: Pure Appl. Opt. **7**, 56 (2005).
[41] J. W. Cahn and J. E. Hilliard, J. Chem. Phys. **28**, 258 (1958).
[42] D. Korteweg and G. de Vries, Philos. Mag. **39**, 422 (1895).
[43] K. Ouchi and H. Fujisaka, Phys. Rev. E **54**, 3895 (1996).
[44] R. Gallego, M. San Miguel, and R. Toral, Phys. Rev. E **61**, 2241 (2000).
[45] G. L. Oppo, A. J. Scroggie, and W. J. Firth, Phys. Rev. E **63**, 066209 (2001).
[46] D. Gomila, P. Colet, M. San Miguel, A. J. Scroggie, and G.-L. Oppo, IEEE J. Quantum Electron. **39**, 238 (2003).
[47] S. M. Tobias, M. R. E. Proctor, and E. Knobloch, Physica D **113**, 43 (1998).
[48] A. S. Landsberg and E. Knobloch, Phys. Lett. A **159**, 17 (1991).
[49] E. Knobloch and J. DeLuca, Nonlinearity **3**, 975 (1990).
[50] C. Martel and J. M. Vega, Nonlinearity **9**, 1129 (1996).
[51] C. Martel and J. M. Vega, Nonlinearity **11**, 105 (1998).
[52] E. Knobloch, in *Nonlinear Dynamics and Pattern Formation in the Natural Environment*, edited by A. Doelman and A. van Harten, Pitman Research Notes in Mathematics, Vol. 335 (Longman, Harlow, Essex, UK, 1995), pp. 130–146.
[53] H. Riecke and L. Kramer, Physica D **137**, 124 (2000).
[54] A. Amengual, E. Hernández-García, R. Montagne, and M. San Miguel, Phys. Rev. Lett. **78**, 4379 (1997).
[55] L. Gelens and E. Knobloch, Phys. Rev. E **80**, 046221 (2009).
[56] C. Beaume, A. Bergeon, and E. Knobloch, Phys. Fluids **23**, 094102 (2011).
[57] A. A. Nepomnyashchy, Physica D **86**, 90 (1995).
[58] J. H. P. Dawes and M. R. E. Proctor, Proc. R. Soc. A **464**, 923 (2008).
[59] A. A. Golovin, A. A. Nepomnyashchy, S. H. Davis, and M. A. Zaks, Phys. Rev. Lett. **86**, 1550 (2001).
[60] G. B. Whitham, *Linear and Nonlinear Waves* (Wiley, New York, 1974).
[61] A. J. Bernoff, Physica D **30**, 363 (1988).
[62] Y. S. Kivshar and B. A. Malomed, Rev. Mod. Phys. **61**, 763 (1989).
[63] H. Aspe and M. C. Depassier, Phys. Rev. A **41**, 3125 (1990).
[64] V. I. Nekorkin and M. G. Velarde, Int. J. Bifurcation Chaos Appl. Sci. Eng. **4**, 1135 (1994).
[65] T. Kawahara, Phys. Rev. Lett. **51**, 381 (1983).
[66] D. E. Bar and A. A. Nepomnyashchy, Physica D **86**, 586 (1995).
[67] D. Tseluiko, S. Saprykin, C. Duprat, F. Giorgiutti-Dauphiné, and S. Kalliadasis, Physica D **239**, 2000 (2010).
[68] V. I. Karpman and E. M. Maslov, Sov. Phys. JETP **46**, 281 (1977).
[69] J. Mason and E. Knobloch, Physica D **205**, 100 (2005).
[70] A. Spina, J. Toomre, and E. Knobloch, Phys. Rev. E **57**, 524 (1998).
[71] A. Podolny, M. A. Zaks, B. Y. Rubinstein, A. A. Golovin, and A. A. Nepomnyashchy, Physica D **201**, 291 (2005).
[72] S. J. Watson, F. Otto, B. Y. Rubinstein, and S. H. Davis, Physica D **178**, 127 (2003).
[73] A. Bergeon and E. Knobloch, J. Phys.: Conf. Ser. **216**, 012001 (2010).
[74] S. M. Houghton, E. Knobloch, S. M. Tobias, and M. R. E. Proctor, Phys. Lett. A **374**, 2030 (2010).